Chapter 5 Aerosol-radiation interactions

Nicolas Bellouin
Department of Meteorology, University of Reading, Reading, UK

Hongbin Yu
NASA Goddard Space Flight Center, Greenbelt, USA

Contents

Long summary

Aerosol-radiation interactions refer to absorption, scattering, and emission of electromagnetic radiation by atmospheric aerosol particles. Scattering refers to a change in the direction of propagation of an electromagnetic wave. Absorption refers to the transformation of electromagnetic energy into internal energy of the particles . Scattering and absorption add up to extinction, or attenuation, of radiation. Emission is the opposite transformation to absorption. Only the coarser particles, like mineral dust and sea spray, emit a sizeable amount of radiation, in the terrestrial part of the electromagnetic spectrum.

Aerosol particles are commonly assumed to be homogeneous spheres in the context of aerosol-radiation interactions. Under this approximation, Mie theory is used to describe mathematically the scattering and absorption of solar and terrestrial radiation. It finds that for a single particle the probability of scattering and absorption, their variations with wavelength, and the angular dependence of scattering depend on only two numbers. The first is the ratio of particle radius to wavelength, called the size parameter . The second is the complex refractive index of the aerosols, which depends on their chemical composition. Wavelength-dependent aerosol properties calculated by Mie theory are the optical depth, which quantifies vertically integrated scattering and absorption by aerosol; the single-scattering albedo, which gives the contribution of scattering to extinction; and the phase function, which calculates the angular dependence of scattering.

The dependence of particle optical properties on the particle size distribution and refractive index means that different aerosol types, and mixtures of types, exhibit a wide spectrum of scattering and absorption efficiencies. In turn, aerosol optical properties are a way to identify aerosol types in the atmosphere based on their interactions with radiation, using remote sensing instruments. In planetary atmospheres, aerosol-radiation interactions translate into a change in the spatial and temporal distribution of radiative fluxes. This change, quantified against a hypothetical atmosphere without aerosol, is called the radiative effect of aerosol-radiation interactions. That radiative effect depends on particle concentrations and optical properties, being in the first order proportional to the aerosol optical depth and single-scattering albedo. But it also depends on environmental factors like the angle of incidence of incoming radiation, the reflectance of underlying surfaces, the presence of clouds, and atmospheric temperature and humidity. The aerosol radiative effect may be positive (gain of energy) or negative (loss of energy) depending on the type, amount, and location of the aerosol. Conversely, the aerosol radiative effect triggers changes in the atmospheric state called rapid adjustments. Those changes are driven by absorption of radiation by the particles, which modifies the atmospheric profiles of temperature and humidity, and consequently cloud formation.

In the solar spectrum and on a global average, present-day aerosol in the Earth's atmosphere increases the amount of solar radiation reflected to space by about 2 W m^{-2}, or 2% of total reflected flux. The radiative effect of aerosol-radiation interactions is therefore negative as it translates in a loss of energy for the Earth system. Aerosol decreases the amount of solar radiation reaching the surface by 6 W m^{-2} (or 3% of total downward flux) and increases the amount of solar radiation absorbed in the atmosphere

by about 4 W m^{-2} (or 5% of total atmospheric absorption.) The radiative effect of aerosol-radiation interactions closely follows the distribution of aerosol optical depth, but its magnitude is decreased over bright surfaces, like deserts and snow- and ice-covered surfaces, and above clouds. In those conditions, aerosol absorption switches the sign of the radiative effect to positive. The aerosol radiative effect in the terrestrial spectrum is mostly exerted by mineral dust. Although it can exceed tens of Watts per square metre in the dustier regions, its global average is small at a few tenths of a Watt per square metre.

All these estimates of aerosol radiative effects are uncertain. From a remote sensing perspective, aerosol retrievals are more accurate in the absence of clouds and over dark surface, like oceans, although the ability to retrieve aerosols above clouds has recently improved. The aerosol optical depth is the most accurate aerosol remote sensing product, but its uncertainties may still translate in uncertainties of about 1 W m^{-2} in aerosol radiative effect. Global retrievals of aerosol single-scattering albedo are more difficult to make and contribute further uncertainties. From a modelling perspective, the simulated aerosol radiative effect suffers from a chain of uncertainties that affect the modelled particle size distribution and chemical composition. In both cases, non-aerosol sources of uncertainty include surface reflectance, the optical properties of clouds, and the radiative transfer calculations themselves. The overall uncertainty in aerosol radiative effect exceeds 1 W m^{-2} at the top of the atmosphere.

The radiative forcing of aerosol-radiation interactions is the change in the aerosol radiative effect over the industrial era. Purely scattering aerosols exert a negative radiative forcing at the top of the atmosphere, thus predicting a cooling of the Earth-atmosphere system. The radiative forcing of partially absorbing aerosol may take either sign at the top of the atmosphere, depending on aerosol single-scattering albedo and phase function, and the reflectance of underlying surfaces and clouds. The latest assessment of the radiative forcing of aerosol-radiation interactions bounds it between −0.6 and −0.2 W m^{-2} (68% confidence interval), offsetting just under 10% of long-lived greenhouse gas radiative forcing. This assessment is based on estimates of aerosol radiative forcing from climate models and satellite remote sensing retrievals. Aerosol radiative forcing is affected by the same uncertainties as the radiative effect, and also by uncertainties in the preindustrial aerosol state, which has not been observed.

5.1. Fundamental aspects of aerosol interactions with radiation

This section summarises the nature of electromagnetic radiation before discussing and describing mathematically the physical processes underlying the interactions between aerosol particles and electromagnetic radiation: scattering, absorption, and emission.

5.1.1. Radiation

Electromagnetic radiation is a continuum of energy emitted by accelerating, electrically charged particles and by electronic transitions within atoms and molecules. Electromagnetic radiation is classically described by Maxwell's equations as electromagnetic waves made of a pair of oscillating, orthogonal electric and magnetic fields. In that description, an electromagnetic wave is characterised by its intensity, its wavelength or frequency, and its phase. Quantum theory provides the alternative view of electromagnetic radiation as being carried by mass-less photons, which is helpful to understand the absorption aspects of aerosol-radiation interactions.

The electromagnetic spectrum is traditionally divided into different regions, from gamma radiation (short wavelength, high energy) to radio waves (long wavelength, low energy). For most atmospheric processes only the ultraviolet, visible, infrared, and microwave parts of the spectrum are relevant (Table 5.1). These regions of the spectrum cover solar and terrestrial radiation, also referred to in the atmospheric science community as shortwave and longwave radiation.

Part of the spectrum	Wavelength boundaries (μm)	Aerosol scattering regime
Ultraviolet	0.01—0.4	Mie
Visible	0.4—0.7	Mie
Near Infrared	0.7—2.5	Mie
Thermal infrared	8—15	Mie/Rayleigh
Microwave	> 1000	Negligible

Table 5.1. Approximate wavelength boundaries and aerosol scattering regime of the parts of the electromagnetic spectrum used in the atmospheric sciences.

Solar radiation is emitted at the surface of the Sun, which has an effective temperature of about 5700 K. This temperature translates, according to Wien's displacement law, into a wavelength of peak emission around $0.5\ \mu m$ ($5 \times 10^{-7}\ m$). The spectrum of solar radiation ranges from about $0.25\ \mu m$ in the ultraviolet to $4\ \mu m$ in the infrared, spanning the entire visible spectrum. The Earth's atmosphere presents an atmospheric window over the visible spectrum, where gaseous absorption is low, allowing a large fraction of incoming solar radiation to reach the surface in the absence of clouds and aerosols.

Terrestrial radiation is emitted by the Earth's surface and atmosphere. It peaks in the infrared part of the spectrum, between 8 and $10\ \mu m$, for an effective temperature of around 288 K. The spectrum of terrestrial radiation ranges from about $3\ \mu m$ in the infrared to millimetre and centimetre wavelengths in the microwave. Like solar radiation, peak emission of terrestrial radiation occurs in an atmospheric window, characterised by low gaseous absorption, which covers the range of infrared wavelength between 8 and $13\ \mu m$. This allows about half of the terrestrial radiation emitted by the surface and atmosphere to escape to space, almost balancing the net incoming solar radiation in the Earth's energy budget (Stephens et al. 2012).

5.1.2. Scattering

Scattering refers to a change in the direction of propagation of an electromagnetic wave. In the atmosphere, scattering is in most cases an elastic process, so the wavelength of the radiation is unchanged. Inelastic scattering, called Raman scattering, where the photon loses energy to the scattering particle, also occurs in the atmosphere, but its likelihood is several orders of magnitude smaller than that of elastic scattering. Because of its rarity, Raman scattering will not be discussed in this chapter but is usefully exploited in lidar measurements of aerosol profiles (Chapter 15).

5.1.2.1. Scattering regimes

There are four scattering regimes, which mathematically correspond to different simplifications of the solutions of Maxwell's equations of electromagnetism (Hansen and Travis, 1974). The regime in which an aerosol particle scatters radiation depends on the ratio between the circumference of the particle and the wavelength of the radiation, λ. For a spherical particle of radius r, that ratio is called the size parameter:

$$x = \frac{2\pi r}{\lambda} \qquad 5.1$$

Table 5.1 summarises the scattering regimes experienced by aerosol particles in different parts of the electromagnetic spectrum, assuming particle sizes ranging from tens of nanometres to tens of microns (Chapter 3). The most relevant scattering regime for aerosol particles, and the focus of the remainder of this chapter, is Mie scattering (Box 5.1). Mie theory is an exact solution of Maxwell equations for homogeneous spheres. Many atmospheric particles, especially soluble particles, can be assumed spherical and homogeneous to a good approximation. Coarse insoluble particles, such as mineral dust, are non-spherical. Numerical methods to compute scattering of radiation by non-spherical particles have been developed, the main one being the T-matrix computation (Waterman, 1965; Mishchenko et al., 1996). Inhomogeneities within a particle can be represented by mixing rules that estimate an effective refractive index from the refractive indices of the constituents of the mixture (e.g. Stier et al.

2007). Although Mie theory is valid for any value of the size parameter x, it is commonly applied to parts of the spectrum where simpler solutions do not apply, typically where $10^{-1} < x < 10^{3}$. In that range of size parameters, $r \sim \lambda$ and different parts of a particle experience different phases of the electric field.

5.1.2.2. Scattering cross section and efficiency factor

For a single aerosol particle, the probability of scattering of radiation at a given wavelength is measured by the scattering cross-section, noted σ_{sca}, in m^2. Provided that the particles are isotropic homogeneous spheres of radius r, Mie theory finds that σ_{sca} depends only on the size parameter, x, (Equation 5.1) and the complex refractive index of the particle, $m = n_r - i\, n_i$ (Box 5.1).

Scattering is conveniently expressed in terms of the scattering efficiency factor, defined as the ratio between the particle scattering cross section and its geometric cross section:

$$Q_{sca} = \frac{\sigma_{sca}}{\pi r^2} \qquad 5.2$$

Figure 5.1 shows the variation of Q_{sca} with size parameter x for three values of the real part of the refractive index: $n_r = 1.33$, 1.53, and 1.75, which correspond to typical values for water, sulfate, and soot, respectively, at visible wavelengths. The imaginary part is set to zero, its effect will be explored in Section 5.1.3. Q_{sca} experiences a series of extrema. The main extrema correspond to constructive and destructive interferences between diffracted and transmitted radiation. The smaller extrema, called "ripples" by Hansen and Travis (1974), correspond to radiation that interacts only with the surface of the particle without propagating through the particle. The maximum value of Q_{sca} occurs for $x \sim 3$ to 6, or $r \sim \lambda$. It follows that accumulation-mode aerosol is most efficient at scattering solar radiation, while coarse-mode aerosol is most efficient at scattering terrestrial radiation. At the Rayleigh limit where $x \ll 1$, Q_{sca} becomes proportional to x^4. At the geometric optics limit where $x \gg 1$, Q_{sca} tends towards 2. Increasing the real part of the refractive index increases the value of the maxima and shifts the position of the extrema to smaller size parameters.

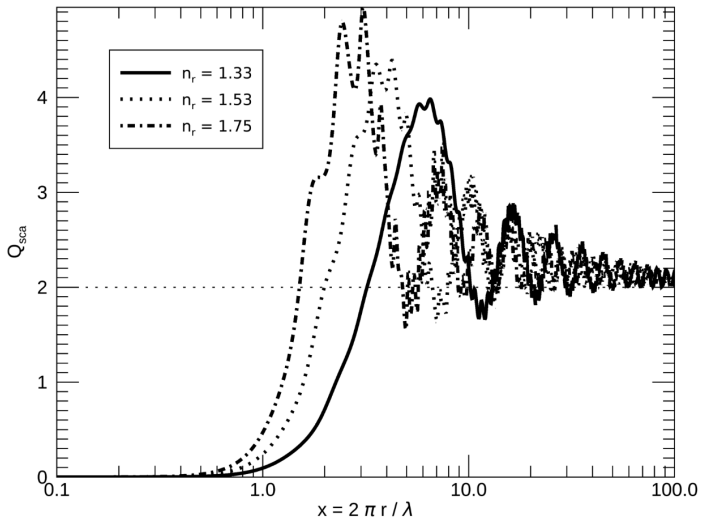

Figure 5.1. Efficiency factor for scattering, Q_{sca}, as a function of the particle size parameter $x = \frac{2\pi r}{\lambda}$. The real part of the refractive index is $n_r = 1.33$ (solid line), 1.53 (dashed), and 1.75 (dot-dashed). The imaginary part is $n_i = 0$.

The effective radius, r_{eff}, is the area-weighted mean radius of an aerosol population and can be used in place of r in the size parameter x:

$$r_{eff} = \frac{\int_0^\infty r\, \pi\, r^2\, n(r)\, dr}{\int_0^\infty \pi\, r^2\, n(r)\, dr} \qquad 5.3$$

where $n(r)$ is the number size distribution function, so that $n(r)\,dr$ is the particle number concentration per unit volume between r and $r + dr$. Surface area and volume size distributions can also be used for similar purposes.

The scattering efficiency factor is in that case

$$Q_{sca} = \frac{\int_0^\infty \sigma_{sca}(r)\, n(r)\, dr}{\int_0^\infty \pi r^2\, n(r) dr} \quad 5.4$$

Wider size distributions incorporate a larger range of particle sizes with varying scattering efficiencies, which has the effect of smoothing out the extrema and ripples seen in Figure 5.1 and to decrease the maximum scattering efficiency.

The volume scattering coefficient β_{sca}, in m^{-1} is commonly used in the aerosol remote sensing community and is defined as:

$$\beta_{sca} = \int_0^\infty \sigma_{sca}(r)\, n(r)\, dr \quad 5.5$$

The mass scattering coefficient, k_{sca}, in $m^2\ kg^{-1}$ (also called the specific scattering coefficient) is preferred by the aerosol modelling community because models often express particle mass concentrations in terms of the mass mixing ratio in dry air (Section 5.4.1). k_{sca} is defined as:

$$k_{sca} = \frac{1}{\rho} \int_0^\infty \sigma_{sca}(r)\, n(r)\, dr \quad 5.6$$

where ρ is the mass density of the particle.

5.1.2.3. Phase function, asymmetry factor, and upscatter fraction

Scattering affects the direction of propagation of electromagnetic waves, so there is a need to quantify the angular aspects of the process. Figure 5.2 describes the geometry of the problem. Incident radiation comes from the Sun with a solar zenith angle θ_s with respect to the local vertical and an azimuth angle ϕ_s. It is then scattered into the scattered direction, which is characterised by its zenith and azimuth angles θ_v and ϕ_v, respectively. The angle between the incident and scattered directions is called the scattering angle and denoted Θ. It is calculated by:

$$cos\ \Theta\ = -\ cos\ \theta_s\ \ cos\ \theta_v\ -\ \ sin\ \theta_s\ \ sin\ \theta_v\ \ cos\ (\phi_s - \phi_v) \quad 5.7$$

Θ is equal to 0 radians for fully forward scattering, and $-\pi$ radians for fully backward scattering.

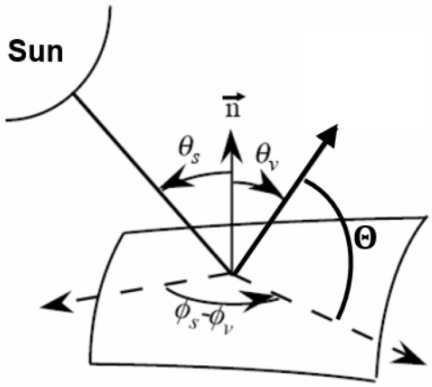

Figure 5.2. Geometry of a scattering event. θ_s and ϕ_s are the solar zenith and azimuth angles, respectively. $\vec{n}$ is the local vertical direction. θ_v and ϕ_v are the scattered zenith and azimuth angles. Θ is the scattering angle. Adapted from Vermote et al. (1997).

The **phase function**, denoted $P(\Theta)$, gives the probability of radiation at a given wavelength to be scattered by a particle with a scattering angle Θ. The probability of being scattered in any direction corresponds to the solid angle of a sphere, 4π, so the phase function is normalised as

$$\int_0^{2\pi} \int_{-1}^{1} P(\Theta)\, d\ cos\,\Theta\ d\phi = 4\pi \qquad 5.8$$

where the phase function has been assumed to be rotationally symmetric, i.e. independent of the azimuth angle ϕ. This assumption is true for a spherical particle.

Figure 5.3a shows two examples of phase functions, one for a spherical particle and the other for non-spherical Saharan mineral dust. In both cases, the phase function exhibits a very strong forward peak, several orders of magnitude larger than the phase function at side-scattering angles: aerosol particles mostly scatter forward. In the spherical case, the phase function exhibits a deep minimum at side-scattering angle (ranging from 60 to 140°) before peaking again in the backward scattering direction, a feature that contributes to the formation of glories. In the non-spherical case, the phase function remains fairly constant over a wide range of side- and back-scattering angles and does not exhibit a glory.

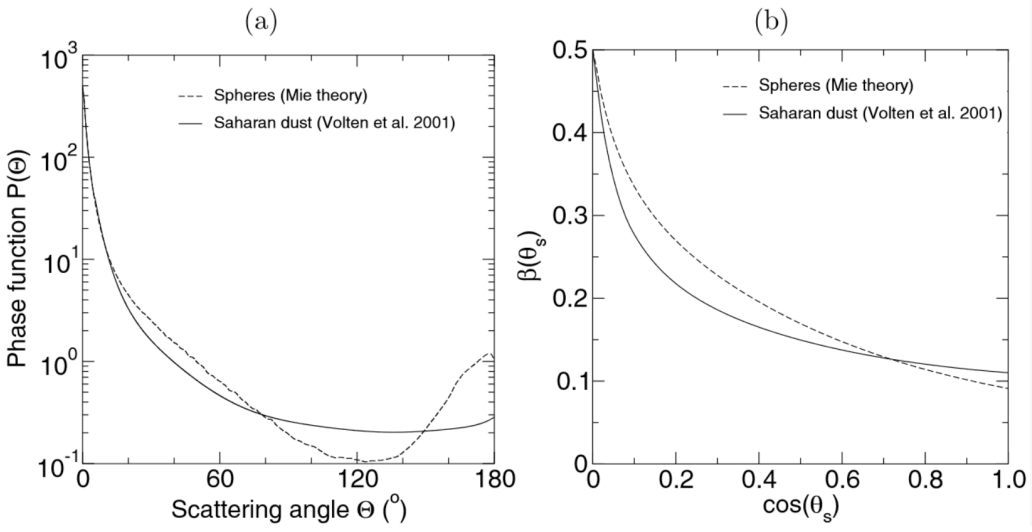

Figure 5.3. (a) Scattering phase function of non-spherical Saharan mineral dust particles measured by Volten et al. (2001) (solid line) and corresponding spherical model (dashed line) at 0.6328 μm as a function of the scattering angle. The forward peaks are assumed to be the same for the two phase functions. Both phase functions are normalized to 4π. (b) Upscatter fraction as a function of the

cosine of the solar zenith angle for the spherical and non-spherical cases. Taken from Bellouin et al. (2004).

The phase function of a population of particles described by its number size distribution function $n(r)$ is given by the scattering-weighted mean:

$$P(\Theta) = \frac{\int_0^\infty \sigma_{sca}\, P(\Theta, r)\, n(r)\, dr}{\int_0^\infty \sigma_{sca}(r)\, n(r)\, dr} \quad 5.9$$

The asymmetry factor, g, is useful in many applications, and especially radiative transfer codes (see section 5.4.1). It is the mean cosine of the scattering angle weighted by the phase function:

$$g = \int_0^{2\pi} \int_{-1}^{1} cos\ \Theta\ P(\Theta)\ \mathrm{d}cos\ \Theta\ d\phi \quad 5.10$$

The value of g is 0 for a particle that scatters with equal probability in the forward ($\Theta > 0$) and backward ($\Theta < 0$) directions, and 1 for a particle that scatters only in the forward direction. Atmospheric aerosols typically have $0.5 < g < 0.9$ at visible wavelengths, with coarser particles having larger asymmetry factors. Note however that g is, by construction, very sensitive to the forward peak of the phase function: in spite of their differences at side-scattering angles, the two phase functions shown in Figure 5.3a share the same asymmetry factor of 0.7 because they share the same forward peaks. So simplifying the phase function into its asymmetry factor leads to errors in radiative transfer calculations.

Like the phase function, the asymmetry factor of an aerosol population described by its number size distribution $n(r)$ is given by its scattering-weighted mean:

$$g = \frac{\int_0^\infty \sigma_{sca}\, g(r)\, n(r)\, dr}{\int_0^\infty \sigma_{sca}(r)\, n(r)\, dr} \quad 5.11$$

The upscatter fraction, β, is the fraction of radiation that a particle scatters into the upward hemisphere. That radiation may be scattered back to space, therefore representing a loss of energy for the Earth system. β is therefore important for quantifying the contribution of aerosol-radiation interactions to the Earth's radiative budget (Section 5.3). It is defined as:

$$\beta(\theta_s) = \frac{1}{4\pi} \int_0^{2\pi} \int_0^{1} cos\ \Theta\ P(\Theta)\ \mathrm{d}cos\ \Theta\ d\phi \quad 5.12$$

The upscatter fraction depends on solar zenith angle θ_s because a larger fraction of forward-scattered radiation is scattered upward with increasing θ_s. Figure 5.3b shows the zenith dependence of the upscatter fractions for the two phase functions shown in Figure 5.3a. The better balance of probability between forward and side-scattering of non-spherical particless increases the upscatter fraction for solar zenith angles smaller than 45° (cosine of 0.7) but decreases it at larger zenith angles.

5.1.3. Absorption

Absorption refers to the transformation of electromagnetic radiation into internal energy of the absorber, mostly heat but also chemical energy. Local heating alters atmospheric temperature and stability and thereby affects cloud properties, resulting in an adjustment to the initial radiative perturbation (section 5.4.4. Effective radiative forcing). Absorption occurs at the molecular level and is explained by quantum physics as the transition of electrons of the molecule to higher quantised energy levels.

5.1.3.1. Absorption cross section and efficiency factor

Like scattering (Section 5.1.2.2), the probability of absorption by a particle is represented by a cross section, σ_{abs} in m^2. The absorption efficiency factor similarly relates that absorption cross section to the geometric cross section of the particle, assumed spherical with radius r:

$$Q_{abs} = \frac{\sigma_{abs}}{\pi r^2} \quad 5.13$$

Figure 5.4 shows Q_{sca} and Q_{abs} for a single particle with an imaginary part of the refractive index n_i increasing from 0 to 1. The real part of the refractive index remains constant at $n_r = 1.53$. Increasing n_i has two effects on Q_{sca}: interference extrema and ripples are smoothed out and Q_{sca} tends towards 1 for large size parameters, instead of towards 2 in the non-absorbing case. As expected, Q_{abs} is zero for $n_i = 0$. For $n_i > 0$, Q_{abs} increases with increasing size parameter, until it reaches a maximum. This maximum is stronger, and located at decreasing values of x, for increasing n_i.

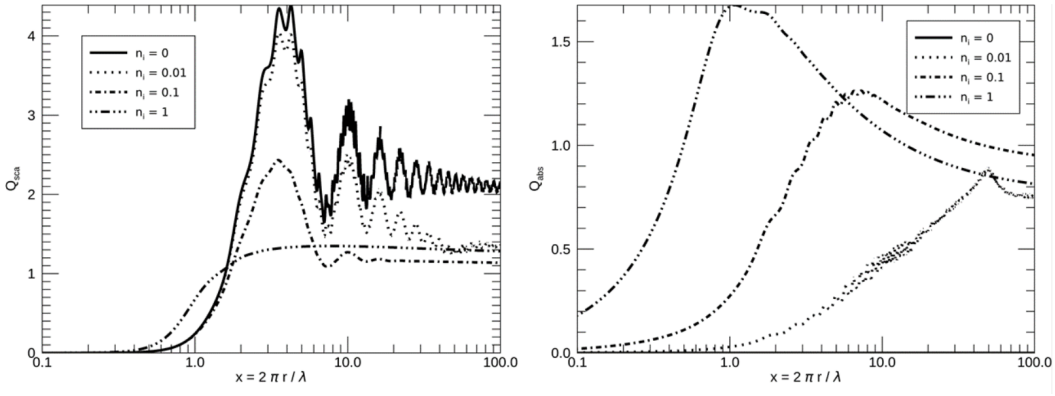

Figure 5.4. Efficiency factor for scattering, Q_{sca} (left), and absorption, Q_{abs} (right), as a function of the size parameter $x = \frac{2\pi r}{\lambda}$. The real part of the refractive index is fixed at $n_r = 1.53$ and the imaginary part takes values of 0 (solid line), 0.01 (dashed), 0.1 (dot dashed), and 1 (dot-dot-dashed).

Particles with a n_i large enough to exert sizeable absorption at solar wavelengths include black carbon, some organic materials called brown carbon (which is mostly emitted from wildfires), and mineral dust. The value of n_i is also important for absorption of longwave terrestrial radiation, but the impact of aerosol is generally much weaker than that of gaseous absorption, unless the aerosol is sufficiently elevated to re-emit the radiation into an atmosphere that is much colder than the surface. Elevated mineral dust plumes or stratospheric aerosols are two cases where terrestrial absorption has an impact on the Earth's budget.

5.1.4. Extinction

Both scattering and absorption represent a loss of energy from the point of view of an observer of incident electromagnetic radiation. It therefore makes sense to consider the two processes together in a process called extinction. The extinction cross section, efficiency factor, and volume and specific extinction coefficients are simply given by:

$$\sigma_{ext} = \sigma_{sca} + \sigma_{abs} \quad 5.14$$

$$Q_{ext} = Q_{sca} + Q_{abs} \quad 5.15$$

$$\beta_{ext} = \beta_{sca} + \beta_{abs} \quad 5.16$$

$$k_{ext} = k_{sca} + k_{abs} \quad 5.17$$

5.1.4.1. Optical depth

The extinction aerosol optical depth, noted τ_a and commonly shortened to aerosol optical depth, is the column-integrated extinction and directly quantifies the strength of aerosol-radiation interactions at a given location. Optical thickness is very often used as a synonym for optical depth, especially for satellite retrievals.

Optical depth is an extensive property as it depends on the amount of aerosol. Its mathematical definition is:

$$\tau_a = \int_0^\infty \beta_{ext}(z)\, dz = \int_0^\infty k_{ext}(z)\, \rho(z)\, dz \qquad 5.18$$

where z denotes the vertical height, from 0 at the surface to ∞ at the top of the atmosphere. Like all quantities discussed in this section, the optical depth depends on wavelength. Typical ranges for τ_a at 0.55 μm (green colour, visible spectrum) obtained by aerosol remote sensing (e.g. Dubovik et al. 2002) are 0.05 to 0.10 in clean remote oceanic regions, 0.1 to 1.0 in polluted industrial cities, and in excess of 2 in wildfire plumes and sandstorms. The water that constitutes soluble aerosols exerts a sizeable fraction of the optical depth.

Scattering and absorption optical depths can be defined in the same way by integrating the scattering and absorption coefficients, respectively, in which case:

$$\tau_{a,ext} = \tau_{a,abs} + \tau_{a,sca} \qquad 5.19$$

The approximate wavelength dependence of τ_a is described by the Ångström exponent (α), named after the Swedish scientist Anders Ångström (1888-1981). It assumes that optical depth depends on wavelength through a power law:

$$\tau_a(\lambda_1) = \tau_a(\lambda_2) \times \left(\frac{\lambda_1}{\lambda_2}\right)^{-\alpha} \qquad 5.19a$$

where λ_1 and λ_2 are two wavelengths (mathematically α is independent of whether $\lambda_1 > \lambda_2$ or vice versa). The Ångström exponent is therefore

$$\alpha = -\frac{\frac{log\ \tau_a(\lambda_1)}{log\ \tau_a(\lambda_2)}}{\frac{log\ \lambda_1}{log\ \lambda_2}} \qquad 5.20$$

The Ångström exponent is mostly used as a first-order indication of the effective size of an aerosol population: the larger the Ångström exponent, the smaller the mean aerosol particle radius. The relationship between Ångström exponent and aerosol size is however not unique because Mie scattering and absorption properties are also affected by the refractive index. Rayleigh scattering is associated with the largest Ångström exponent of 4. Since atmospheric particles are mostly found in the Mie scattering regime, their Ångström exponents are smaller, varying between 0 and 2.5. Coarse particles may exhibit negative Ångström exponents. Equation 5.20 can also be applied to $\tau_{a,sca}$ and $\tau_{a,abs}$ to define the scattering Ångström exponent, α_{sca}, and absorption Ångström exponent, α_{abs}, respectively. The absorption Ångström exponent is useful to distinguish between different types of absorbing aerosols (Section 5.2.1).

An alternative measure of particle size is the fine-mode fraction, which is the fraction of $\tau\ a$ that is exerted by particles with radii smaller than 0.5 μm. The fine-mode fraction is retrieved from sun-photometer measurements of the spectral and angular dependence of scattered radiance (Dubovik and King, 2000) and from satellite measurements of radiance at multiple wavelengths (e.g. Remer et al., 2005).

5.1.4.2. Single-scattering albedo

The single-scattering albedo quantifies the fraction of extinction due to scattering. It is an intensive aerosol property as it is not directly related to the amount of aerosols. It is defined as:

$$\varpi_0 = \frac{\sigma_{sca}}{\sigma_{ext}} = \frac{\sigma_{sca}}{\sigma_{sca} + \sigma_{abs}} = 1 - \frac{\sigma_{abs}}{\sigma_{ext}} \quad 5.21$$

Equation 5.21 can also be written in terms of scattering and extinction efficiencies, volume scattering and extinction coefficients, and specific scattering and extinction coefficients. Similarly, a column-integrated ϖ_0 is obtained by:

$$\varpi_0 = \frac{\tau_{a,sca}}{\tau_{a,ext}} = \frac{\tau_{a,sca}}{\tau_{a,sca} + \tau_{a,abs}} = 1 - \frac{\tau_{a,abs}}{\tau_{a,ext}} \quad 5.22$$

By definition, $\varpi_0 = 1$ indicates that the aerosol or aerosol column is purely scattering, while $\varpi_0 = 0$ indicates pure absorption. Like the optical depth, the single-scattering albedo of particles exhibits strong dependence on the wavelength. Most observed particle mixtures have ϖ_0 larger than 0.7 in the visible spectrum (Section 5.2.1).

Figure 5.5 shows the single-scattering albedo obtained from the calculations of Q_{sca} and Q_{abs} shown on Figure 5.4. The case for $n_i = 0$ is not shown since it implies $\varpi_0 = 1$. The dependence of ϖ_0 on x and n_i is complex: a given n_i can correspond to cases where the contribution of absorption to extinction is relatively small ($\varpi_0 \sim 1$) or much larger, depending on the size parameter. As noted in Hansen and Travis (1974), for relatively small n_i the single-scattering albedo ϖ_0 tends to 0.53 for large x, because geometric optics predicts that 50% of light is diffracted, 3.3% is reflected, while 47.6% is refracted (and absorbed) into the particle.

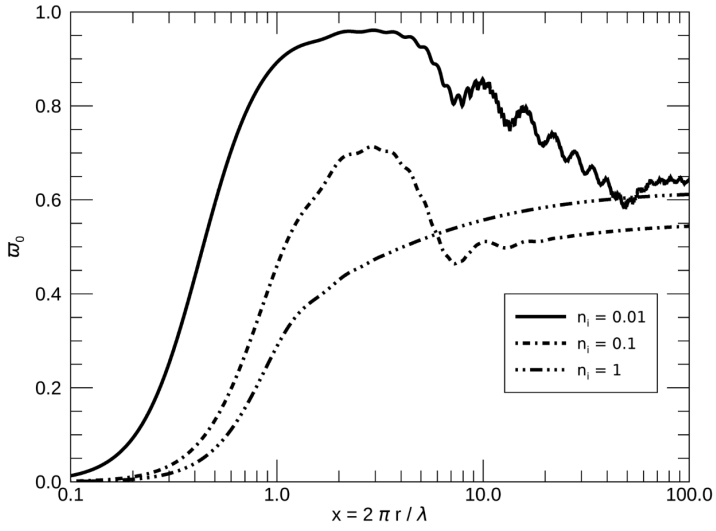

Figure 5.5. Single-scattering albedo ϖ_0 as a function of the size parameter $x = \frac{2\pi r}{\lambda}$. Like in Figure 5.4, the real part of the refractive index is fixed at $n_r = 1.53$ and the imaginary part takes values of 0.01 (dashed), 0.1 (dot dashed), and 1 (dot-dot-dashed).

5.1.5. Emission

Emission is, on a quantic level, the counterpart of absorption, whereby electrons are de-excited to valence shells of lower energies. The absorption cross-section can therefore also be used to characterise emission, as implied by Kirchhoff's law of thermal radiation. On a macroscopic level, the amount of emitted radiation is quantified, for idealised blackbodies, by Planck's law, which only depends on the temperature of the emitting object and the wavelength of the radiation. Aerosol particles have the temperature of the atmospheric layer that carry them, so emit in the terrestrial spectrum.

5.1.6. Aerosols and radiative transfer

Radiative transfer is the science that calculates the distribution of radiative energy in planetary atmospheres based on their composition. It is a branch of optics, thanks to recent theoretical derivations that relate it directly to the Maxwell's equations (Mishchenko, 2014). Radiative transfer calculates spectral radiances and radiative fluxes. Spectral radiance is the mathematical representation of a beam of radiation. It is the amount of energy coming from an infinitesimal solid angle over an infinitesimal interval of wavelengths and crossing an infinitesimal surface during an infinitesimal amount of time. Spectral radiance at wavelength λ, in μm, is denoted here I_λ and given in W m^{-2} μm^{-1} sr^{-1}. Radiative fluxes, F in W m^{-2}, are spectral radiances integrated over all solid angles, and often integrated over solar and terrestrial parts of the electromagnetic spectrum separately. Radiative transfer theory is discussed extensively in the context of small particles by Bohren and Huffman (1998) and Mishchenko et al. (2002).

Aerosol-radiation interactions play four distinct roles in radiative transfer calculations. The first role is exerted by aerosol extinction. According to Beer's law, the extinction optical depth of an aerosol layer decreases the radiance that is transmitted through the layer as:

$$I_\lambda(s_2) = \left(-\frac{\tau_a(\lambda)}{cos\ \theta}\right) = I_\lambda(s_1) \times T_\lambda \qquad 5.21a$$

where I_λ is the spectral radiance at wavelength λ, s_1 and s_2 are the boundaries of the layer, τ_a is the aerosol optical depth (section 5.1.4.1), θ is the zenith angle of the radiation, and T_λ is the transmittance of the layer. The second role is through aerosol absorption (section 5.1.3), which increases overall atmospheric absorption and heating rates (section 5.2.6). The third role is through aerosol scattering (section 5.1.2), which effectively transforms direct radiation coming from the direction of the Sun into diffuse radiation. The fourth role is through aerosol emission. As discussed in section 5.1.5, that role occurs mostly in the infrared.

Figure 5.5b illustrates how aerosol extinction, absorption, and scattering affects solar spectral radiance as it propagates through an aerosol layer. Computing the corresponding aerosol radiative effect involves complex radiative transfer, which needs to also consider molecular scattering, gaseous absorption and emission, reflection and emission by the surface, and scattering, absorption, and emission by clouds (Petty 2006). Aerosol-radiation interactions generally represent a small contribution to total atmospheric transmittance. For example, the optical depth of clouds routinely exceeds that of aerosol by an order of magnitude. Nevertheless, the aerosol contribution to the Earth radiative budget cannot be neglected (section 5.3).

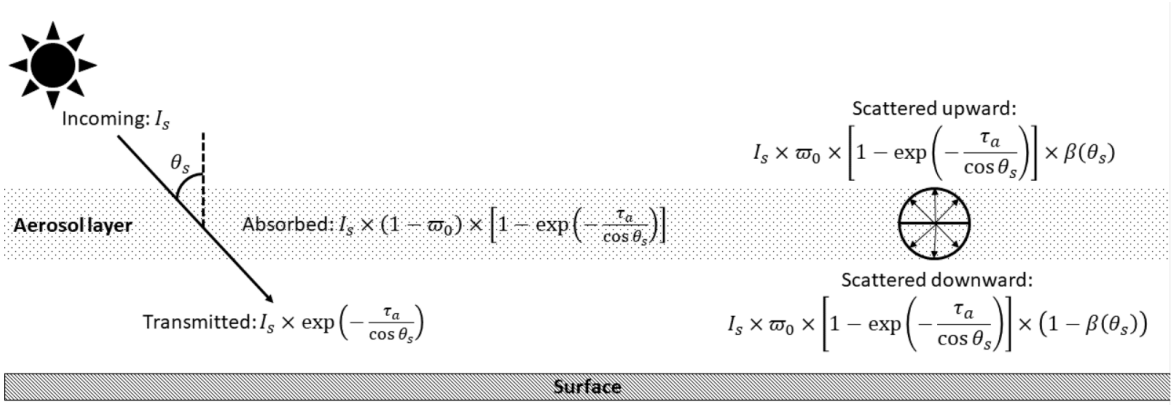

Figure 5.5b. Effects of aerosol-radiation interactions on incoming solar spectral radiance I_s at a solar zenith angle θ_s. τ_a, ϖ_0, and β are the aerosol optical depth, single-scattering albedo, and upscatter fraction, respectively. Note that radiance and particle optical properties depend on wavelength.

Box 5.1: Mie theory

The Mie solutions to Maxwell's equations of electromagnetism, often referred to simply as Mie theory in the aerosol community, have been developed by the German scientist Gustav Mie (1868-1957) in the early years of the 20th century (Mie, 1908). They were found by projecting Maxwell's equations onto homogeneous spheres. Similar solutions, also within Mie theory, exist for stratified spheres and for infinite cylinders, although the latter is of limited use in aerosol science.

For a single particle, Mie theory finds that extinction and scattering efficiencies Q_{ext} and Q_{sca} (section 5.1.2.2) and the phase function P and its asymmetry factor g (section 5.1.2.3) only depend on the size parameter $x = \frac{2\pi r}{\lambda}$, where r is the radius of the spherical particle, and the particle complex refractive index, $m = n_r - i \times n_i$. The real part n_r is the ratio between the velocity of the radiation in a vacuum and the velocity in the particle. The imaginary part n_i measures the degree of attenuation during the propagation through the particle. Both real and imaginary parts depend on the chemical composition of the materials that constitute the particle, including water for soluble aerosols.

Mie theory expresses Q_{ext}, Q_{sca}, and g as infinite series of electric and magnetic multipoles, represented by the complex numbers a_n and b_n, respectively:

$$Q_{ext} = \frac{2}{x^2}\sum_{n=1}^{\infty}(2n+1)\,Re(a_n + b_n) \qquad 5.22$$

$$Q_{sca} = \frac{2}{x^2}\sum_{n=1}^{\infty}(2n+1)(|a_n|^2 + |b_n|^2) \qquad 5.23$$

$$g = \frac{4}{x^2 Q_{sca}}\sum_{n=1}^{\infty}\left[\frac{n(n+2)}{n+1}Re(a_n a_{n+1}^* + b_n b_{n+1}^*) + \frac{2n+1}{n(n+1)}Re(a_n b_n^*)\right] \qquad 5.24$$

where Re denotes the real part of a complex number, and stars denote the complex conjugate. The multipoles a_n and b_n, and hence scattering and extinction efficiencies, only depend on x and the refractive index of the aerosol, m. The scattering phase function is calculated as an infinite series of complex scattering amplitudes, S_1 and S_2, themselves dependent on the multipoles a_n and b_n:

$$P(\Theta) = \frac{r}{x^2 Q_{sca}}(|S_1|^2 + |S_2|^2) \qquad 5.24b$$

The calculation of the multipoles and amplitudes is beyond the scope of this textbook but commonly follows the highly optimised algorithms derived by Wiscombe (1980).

5.2. Factors determining the radiative effect of aerosol-radiation interactions

Aerosol-radiation interactions depend on the optical properties of the particles, but also on environmental factors, including solar zenith angle, surface properties, clouds, and atmospheric temperature and humidity profiles. The aerosol radiative effect of aerosol-radiation interactions quantifies the contribution of aerosol extinction to radiative fluxes. Denoted here F_{ari} and measured in W m^{-2}, it is defined as the difference in radiative fluxes with and without aerosol-radiation interactions:

$$F_{ari} = F_{aer} - F_{no-aer} \quad 5.25$$

where F is the net radiative (incoming minus outgoing) flux in the solar or terrestrial spectrum or both, defined at the top of atmosphere (TOA) or at the surface. Subscripts *aer* and *no-aer* are for atmospheres with and without aerosol. At the TOA and in the solar spectrum, upward scattering by aerosol increases the upward radiative flux compared to an atmosphere without aerosol. In that case, $F_{aer}^{TOA} < F_{no-aer}^{TOA}$ and F_{ari} is negative. Conversely, aerosol absorption decreases the upward radiative flux, leading in some cases to a positive F_{ari}. At the surface, both aerosol scattering and absorption decrease downward radiative flux.

Because of limitations of aerosol remote sensing in the presence of clouds (Chapter 15), F_{ari} has often been quantified separately in cloud-free and cloudy sky, with the overall, all-sky F_{ari} computed as:

$$F_{ari} = F_{ari}^{cloud-free} \cdot (1 - f_{cloud}) + F_{ari}^{cloudy} \cdot f_{cloud} \quad 5.26$$

where f_{cloud} denotes the cloud fraction. That equation should be applied on local, instantaneous radiative fluxes because both aerosol and clouds vary greatly in time and space and are to a large extent co-varying.

5.2.1. Optical properties of aerosol particle types

The particle optical properties introduced in Section 5.1 depend strongly on particle type. Table 5.2 summarises the physicochemical and optical properties of various aerosols. It is important to note the variability of absorption within a given type. For industrial and biomass-burning aerosols, optical property variability is caused by variations in the fraction and morphology of absorbing black and brown carbon within the particles (or, as an external mixture, within different particles). For mineral dust aerosol, hematite and goethite contribute to the absorption of radiation in the ultraviolet and blue wavelengths. Although emissions of biogenic and biological particles are comparable to other major aerosol species (Chapter 16), knowledge of their physicochemical and optical properties suffers from a lack of comprehensive measurements.

Aerosol type	Emissions	Main composition	Typical size	Hygroscopicity	Absorption
Industrial/ urban pollution	Mostly gaseous precursors (SO_2, NO_2, NH_3, VOC), also primary (BC, OM)	Sulfate, nitrate, carbonaceous	Sub-micron, some coarse-mode nitrate	High	Strongly variable, depending on relative fraction of carbonaceous material

Biomass burning smoke	Mostly primary (BC, OM), also gaseous precursors (VOCs, SO_2, NO_2)	Carbonaceous	Sub-micron	Hydrophobic at emission, more hydrophilic after ageing	Moderate, depends on combustion temperature and fuel type
Mineral dust	Primary (minerals, including calcite, kaolinite, quartz, feldspar, gypsum, hematite, and goethite)	Minerals	Sub-micron to super-micron, non-spherical	Low	Variable, depending on fraction of hematite and goethite, mainly in UV and blue range
Biogenic and biological	Gaseous precursors (isoprene and terpenes), primary (bacteria, viruses, fungal spores, and pollens)	Biological organisms or their solid fragments, non-spherical and often attached to mineral dust and other particles	Sub-micron	Variable and poorly known	Certain fungal spores can be highly absorbing.
Marine	Primary (inorganic sea salt and organic matter), gaseous precursors (DMS and isoprene)	Sodium chloride, sulfate and organic aerosol	Sub-micron to coarse, with highly variable contribution of sub-micron particles	High	Extremely low
Volcanic	Primary (ash), gaseous precursors (SO_2)	Minerals, sulfate	Sub-micron to coarse	High for sulfate	Sulfate purely scatters, volcanic ashes are absorbing

Table 5.2. Physical and chemical characteristics of the main atmospheric aerosol types that contribute to their optical properties.

Figure 5.6 shows the intensive optical properties of seven aerosol types derived from ground-based sun-photometer measurements (Russell et al., 2014). The optical properties of mineral dust differ substantially from urban-industrial pollution and biomass burning smoke. Mixtures of pollution and mineral dust have optical properties between those types. Marine aerosol is non-absorbing and spherical and has a larger Ångström exponent and fine-mode fraction of the optical depth than mineral dust. Urban-industrial pollution in Asian countries is generally more absorbing than that in countries of North America and Europe. Smoke originating from burning of savannah and grasses (more frequently in the flaming phase) in equatorial Africa is more absorbing than that from burning of rainforest in Amazon basin (more frequently in the smoldering phase).

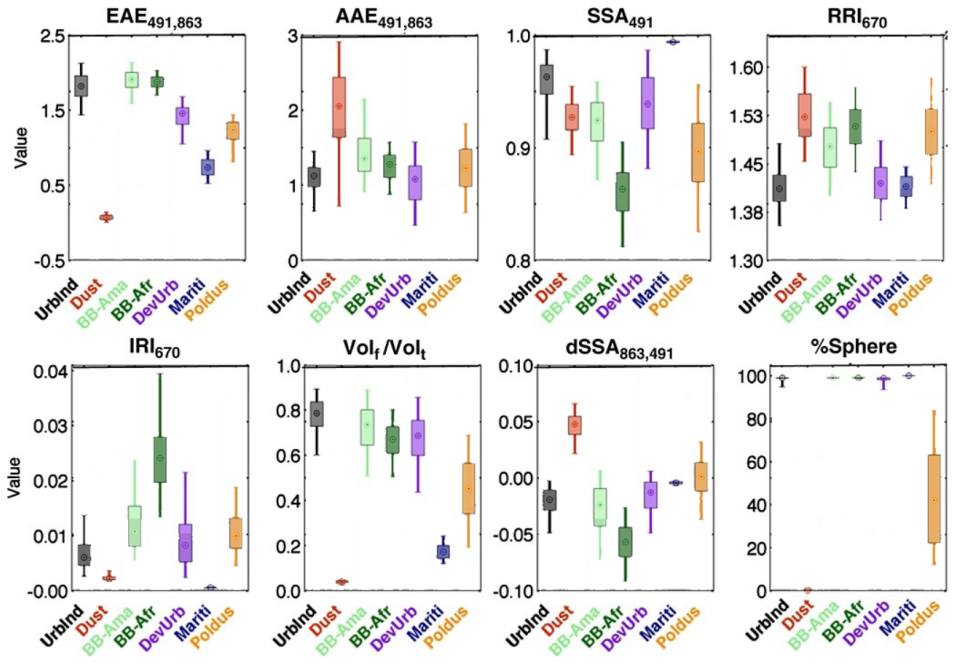

Figure 5.6. Aerosol optical properties represented as box-and-whisker plots (central dot: median value; box; 25th to 75th percentile; whiskers: 5th and 95th percentile) for seven aerosol types. The optical properties shown are: Extinction Ångström Exponent ($EAE_{491\text{-}863}$) and Absorption Ångström Exponent ($AAE_{491\text{-}863}$) calculated between wavelengths of 491 and 863 nm; Single-scattering albedo at 491 nm (SSA491); real and imaginary parts of the refractive index at 670 nm (RRI670 and IRI670); Ratio of fine-mode volume to total volume (Vol_f/Vol_t); difference in single-scattering albedo between 863 and 491 nm ($dSSA_{863\text{-}491}$); and percentage of extinction exerted by spherical (versus non-spherical) particles (%Sphere). The seven aerosol types are Urban Industrial – Developed Economy (UrbInd); Pure mineral dust (Dust); Biomass-burning in the Amazon (BB-Ama); African biomass-burning (BB-Afr); Urban Industrial – Developing Economy (DevUrb); Maritime (Mariti); and Polluted Dust (PolDust). These type-dependent characteristics are derived from sun-photometer observations from the Aerosol Robotic Network (AERONET, Holben et al., 1998). Figure adapted from Figure 6 of Russell et al. (2014).

5.2.2. Solar zenith angle

Figure 5.7 illustrates the dependence of F_{ari} on solar zenith angle θ_s over different land cover types. The dependence arises from the competition between two effects. First, the amount of solar radiation entering the atmosphere and interacting with aerosols is proportional to $cos\,(\theta_s)$ so larger θ_s leads to smaller solar irradiance reaching the aerosol layer. Second, larger θ_s are associated with longer paths over which aerosol interacts with solar radiation. For purely scattering aerosol, F_{ari} at the TOA peaks around θ_s~70° because of the angular dependence of both aerosol upscatter fraction and Rayleigh scattering by atmospheric molecules (Boucher et al., 1998). In contrast, for absorbing aerosol the dependence of F_{ari} on θ_s is relatively weak because aerosol absorption decreases with increasing θ_s, nearly compensating for the dependence of aerosol upscatter on θ_s (Yu et al., 2002). Because of that non-linear dependence on θ_s, one must sample a range of θ_s to calculate an unbiased daily average of F_{ari} (Yu et al., 2004).

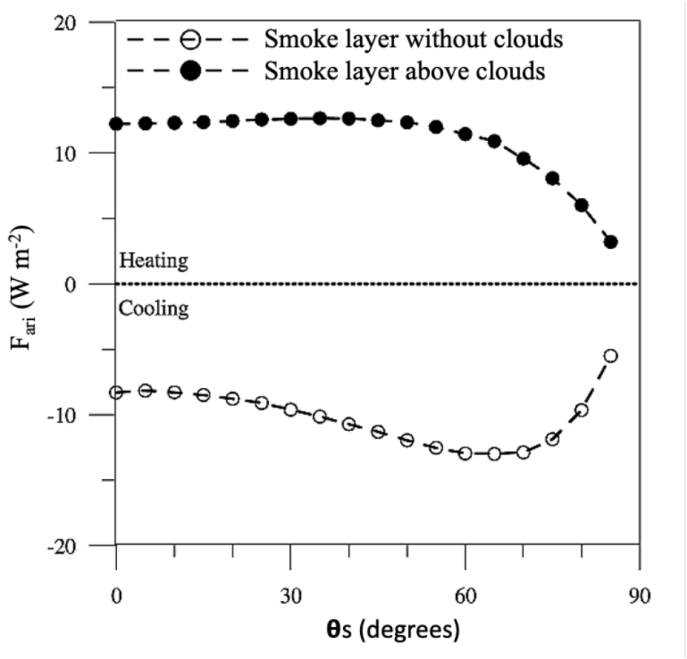

Figure 5.7. Dependence of the radiative effect of aerosol-radiation interactions, F_{ari} in W m^{-2}, on the solar zenith angle θ_s for an elevated biomass burning smoke layer without and with clouds beneath it. The solar spectral range single-scattering albedo is 0.90. Figure adapted from Keil and Haywood (2003).

5.2.3 Underlying surfaces

An accurate representation of surface properties, including surface reflectance, skin temperature, and emissivity, is important for quantifying F_{ari} at the TOA and surface. Surface reflectance is important in the solar spectrum, while surface skin temperature and emissivity determine how much thermal infrared radiation emitted from the surface interacts with mineral dust layers. Multiple reflections between the surface and an aerosol layer cause a non-linear influence of the surface. In general, F_{ari} is more negative over darker surfaces. But even weak aerosol absorption above a highly reflective surface (deserts, snow, or ice) will switch the sign of F_{ari} at the TOA to positive.

The surface reflectance is highly anisotropic and wavelength dependent, so needs to be adequately characterized when calculating the aerosol-radiation interactions. The angular distribution of reflection to the upper hemisphere above a surface is often described by the bidirectional reflectance distribution function (BRDF), an intrinsic property of the surface that depends on texture, structure, and composition of the surface. When calculating F_{ari}, the BRDF is usually simplified to the concept of surface albedo, the ratio of reflected to incident solar radiation, that can be observed from satellites. It is however important to note that the surface albedo is not an intrinsic property of the surface. It involves an integral of BRDF for all combinations of incident and reflection geometry in the upper hemisphere, which depends on atmospheric conditions, including aerosols. Aerosol modifies the directional and spectral composition of incident solar radiation and hence alters the surface reflection and the solar energy budget, adding to F_{ari} (Yu et al., 2004; Bellouin et al., 2004, Derimian et al. 2016). The magnitude of these effects depends strongly on both aerosol properties and land classifications, as illustrated by Figure 5.7.

5.2.4 Influence of clouds

Clouds profoundly modify F_{ari}. The extent of that modification depends on the aerosol and cloud properties, their relative positions in the atmosphere, and on their diurnal variation with respect to the solar illumination (Haywood and Shine, 1997). Cloud properties that must be accounted for include cloud fraction, cloud optical depth and cloud droplet size. For absorbing aerosols, the vertical profile of clouds is also important (Keil and Haywood, 2003).

To a first-order approximation, F_{ari} is negligible beneath overcast skies but is a cloud-fraction weighted product of cloud-free and cloudy sky F_{ari} beneath partly cloudy skies (e.g., Charlson et al., 1992). Such an assumption only holds for optically thick clouds residing above the aerosol layer, when the solar radiation is sufficiently scattered by the cloud. For optically thin clouds, a significant amount of solar radiation is transmitted to, and will interact with, the underlying aerosol layer. If absorbing aerosol lies above the cloud layer, which effectively becomes a very bright surface, then effect of aerosol absorption on the TOA radiative flux tends to be magnified, inducing a positive F_{ari} at the TOA (Section 5.2.3).

5.2.5 Atmospheric temperature and humidity profiles

Atmospheric temperature and humidity profiles affect the aerosol properties and hence F_{ari}. Hygroscopic particles such as sulfate, nitrate, and sea-salt, take up ambient water, a process called hygroscopic growth, which depends strongly on relative humidity (RH) (Chapter 3). Optical properties change because particle size increases with increasing RH and the refractive index also changes. This effect is non-linear with RH and varies with particle chemical composition. For example, as RH increases from 40% to 80%, the scattering cross section of sulfate-dominated aerosol doubles, whereas it increases by only 10-40% for smoke over the same RH range (Hobbs et al., 1997). Particle hygroscopicity also depends on the aging process (Kotchenruther and Hobbs, 1998) – see Ch. 3. The response of the absorption coefficient to increasing RH is uncertain, although theoretical studies indicate it should be much smaller than that for the scattering coefficient. Consequently, for hygroscopic particles, ϖ_0 increases with RH. In addition, g increases with increasing RH because of the increase in particle size.

Atmospheric temperature profiles also influence the terrestrial F_{ari} exerted by mineral dust and other coarse particles. The thermal infrared radiation emitted from the surface is partly scattered back to the surface and partly absorbed by a mineral dust layer. The layer then emits thermal radiation at its own temperature. The difference in temperature between the mineral dust layer and the surface therefore determines the perturbation of outgoing thermal infrared radiation by the dust layer at the TOA. For large mineral dust events, that terrestrial perturbation can reach tens of Watts per square metre (Haywood et al. 2005).

5.2.6 Rapid adjustments to radiative effects

Rapid adjustments are changes to the atmospheric state that occur after a radiative perturbation is imposed, but without a large-scale change in surface temperature (Sherwood et al. 2015) – see Ch. 2. As such, they are now seen as “adjustments” to the radiative effects, rather than part of the climate response to the perturbation, which involves a change in surface temperature that returns the Earth’s energy budget to equilibrium. Aerosol-radiation interactions trigger rapid adjustments because of local changes in surface temperature, and because of the atmospheric response to aerosol absorption. Aerosol absorption modifies the vertical profile of the net radiative flux, thus imposing a heating rate equal to:

$$H(z) = -\frac{1}{\rho(z) \times c_p} \frac{\partial F}{\partial z}(z) \qquad \text{5.26b}$$

where z denotes the height, H is the heating rate, in K day^{-1}, ρ is the air density, and $\frac{\partial F}{\partial z}$ is the divergence of net radiative flux due to aerosol absorption. The specific heat capacity of air at constant pressure is $c_p = 1005$ J kg^{-1} K^{-1}.

The evolution of the atmospheric boundary layer, particularly over land, is directly driven by and rapidly responds to the amount of solar radiation received by the surface. Aerosol scattering and absorption substantially diminishes the surface radiative flux, lowers the surface temperature, and hence reduces the release of surface sensible and latent heat fluxes. The reduction in surface sensible heat flux is greater than that of surface latent heat flux (Yu et al., 2002; Zhang et al., 2008). Local atmospheric heating by aerosol absorption strengthens atmospheric stratification and inhibits turbulent mixing below the aerosol layer along with surface cooling but weakens stratification above the aerosol layer. Overall, these changes inhibit the vertical development of the atmospheric boundary layer (Yu et al., 2002).

The inhibition of atmospheric boundary layer development and/or local heating of the atmosphere resulting from aerosol-radiation interactions may reduce the formation of clouds, an effect commonly called semi-direct effect or "cloud burning" effect (Hansen et al., 1997; Ackerman et al., 2000; Koren et al., 2004; Johnson et al., 2004; Zhang et al., 2008). A decrease in cloud fraction or liquid water content increases solar radiation reaching the surface, yielding a positive semi-direct effect that offsets F_{ari}. However, aerosol primarily located above cloud (e.g., southern African smoke over stratocumulus in Southeast Atlantic Ocean) may increase low cloud cover by strengthening the above-cloud temperature inversion, leading to a negative semi-direct effect on solar radiation. The semi-direct effect shows considerable diurnal variations (Zhang et al., 2008; Herbert et al., 2020). Moreover, given that low-level and high-level clouds have different radiative effects, aerosol heating may influence low- and high-level clouds differently, depending on the vertical profile of aerosol absorption (Bond et al., 2013).

5.3. Radiative effect of aerosol-radiation interactions

The great variations in aerosol optical properties and environmental factors discussed in Section 5.2 lead to large temporal and spatial variability in F_{ari}. Advances in satellite aerosol remote sensing over the last two decades (Chapter 15) have therefore played an important role in quantifying the global magnitude and distribution of F_{ari} and in improving global aerosol models. In the early 2000s when several global retrievals of τ_a from new-generation sensors emerged, these unprecedented aerosol observations allowed increasingly observation-based estimates of $F_{ari}^{cloud-free}$ (Yu et al., 2006; IPCC, 2013). In addition, the record of aerosol vertical distribution from spaceborne lidar observations now covers 15 years.

Satellite characterizations of aerosol microphysical and optical properties including aerosol absorption, particle size and shape, has improved, which allows for mapping aerosol types. The implementation of multispectral, multi-angle, polarization, and lidar techniques has also provided unprecedented opportunities of observing above-cloud aerosol and F_{ari}^{cloudy} (Yu and Zhang, 2013). More recently, aerosol re-analyses have emerged, assimilating satellite retrievals of τ_a into model simulations of the global aerosol system (Inness et al., 2019; Randles et al., 2017).

5.3.1 Radiative effect efficiency of aerosol types

The distinctive optical properties of different aerosol types result in different radiative effects. To first order of approximation, $F_{ari}^{cloud-free}$ is proportional to τ_a. Thus, $F_{ari}^{cloud-free}$ is often normalized by τ_a to quantify the efficiency of aerosol in perturbing radiative fluxes. The normalized $F_{ari}^{cloud-free}$ is often called aerosol radiative effect efficiency and is largely determined by aerosol intensive properties including single-scattering albedo (ϖ_0) and the phase function. Figure 5.8 shows clear-sky solar radiative effect efficiencies at the TOA, surface and in the atmosphere for different aerosol types, based on sun-photometer observations of aerosol optical properties (Zhou et al., 2005). In the solar spectrum and at the TOA, efficiencies are either negative, from about −15 to −40 W m^{-2} τ_a^{-1}, because aerosol scatters radiation back to space, or positive, from about +30 to +70 W m^{-2} τ_a^{-1} because aerosol absorption heats the atmosphere. Both scattering and absorption decrease the amount of radiation reaching the surface, leading to negative efficiencies of about −45 to −100 W m^{-2} τ_a^{-1}. Aerosol is therefore much more efficient at exerting a radiative effect at the surface than at the TOA.

Biomass burning smoke from tropical Africa causes the strongest atmospheric heating and surface cooling per unit τ_a. For mineral dust, the radiative effect is stronger over dark ocean than over bright desert, and its TOA efficiency is smallest for surface albedo around 0.3 to 0.35. The strong dependence of F_{ari} on the aerosol type manifests the importance of accurately quantifying the relative components of aerosol in models, so constraining models with observed τ_a alone does not guarantee realistic efficiencies.

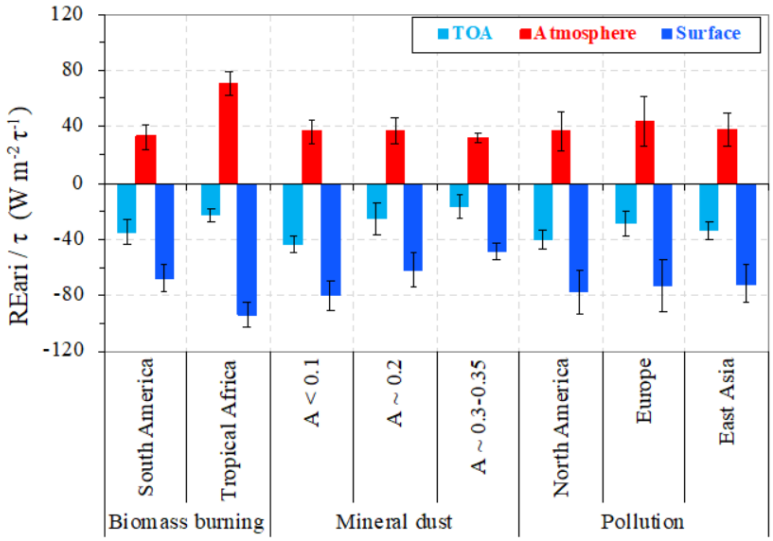

Figure 5.8. Clear-sky and 24-hr average solar radiative effect efficiency (W m^{-2} τ_a^{-1}) at the top of the atmosphere (light blue), in the atmosphere (red), and at the surface (dark blue), as a function of aerosol type as derived from sun-photometer observations. τ_a is the aerosol optical depth at 0.55 μm. For mineral dust, the radiative effect efficiency also depends on broadband surface albedo (A). Figure adapted from Zhou et al. (2005).

5.3.2 Aerosol radiative effect in cloud-free conditions

Estimates of global $F_{ari}^{cloud-free}$ with satellite observations belong to three groups of methods. The first group combines satellite retrievals of τ_a with satellite measurements of TOA radiative fluxes to obtain $F_{ari}^{cloud-free}$ at TOA only and mostly over oceans, where aerosol retrievals are most accurate. This approach does not require assumptions of aerosol optical properties. The second group calculates radiative fluxes using radiative transfer models based on satellite-retrieved τ_a and intensive properties (e.g., ϖ_0). The third group constrains aerosol modelling through data assimilation of satellite-retrieved τ_a. Re-analysed τ_a and model-based aerosol intensive properties, evaluated by surface observations, are used to calculate radiative fluxes.

Figure 5.9 summarizes estimates of global annual mean solar $F_{ari}^{cloud-free}$ by total aerosol, over ocean and land separately. Fewer studies have estimated $F_{ari}^{cloud-free}$ at the surface than at the TOA. Estimates based on active remote sensing by the CALIPSO lidar (Henderson et al., 2013; Matus et al., 2015, 2019; Oikawa et al., 2013, 2018) are significantly smaller than those derived from passive observations. This discrepancy is probably due to different limitations of passive and active aerosol remote sensing. Passive aerosol retrievals of τ_a may be biased high compared to lidar measurements because of cloud contamination. Conversely, active instruments may not be sensitive enough to tenuous aerosol layers or miss the lower section of thick aerosol layers because laser light is completely attenuated by the sections above.

Globally averaged solar $F_{ari}^{cloud-free}$ for the studies presented in Figure 5.9 is −4.1 ±1.6 W m^{-2} (1σ) at the TOA and −8.6 ±1.7 W m^{-2} at the surface, suggesting that aerosols absorb about 4.5 W m^{-2} of solar radiation in cloud-free conditions.

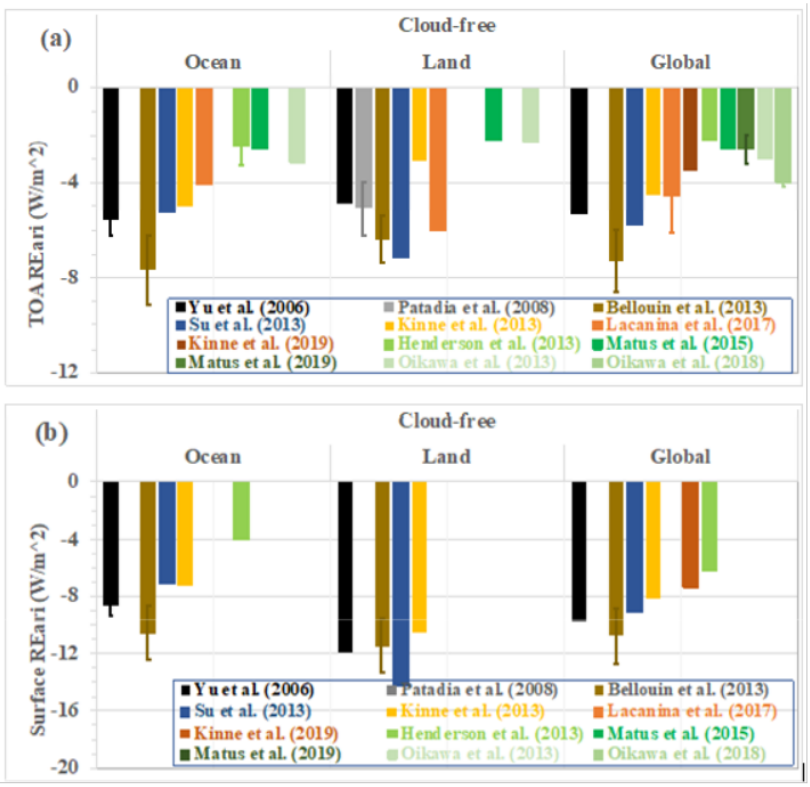

Figure 5.9. Satellite-based estimates of near-global (60°S-60°N), annual mean cloud-free solar aerosol radiative effect at (a) the top of the atmosphere and (b) surface by total aerosol. Estimates are derived from satellite retrievals of aerosol optical depth complemented by satellite observations of radiances/fluxes or aerosol intensive properties from surface observations and/or model simulations. Estimates published before 2006 and reviewed by Yu et al. (2006) are averaged together for the sake of brevity.

Annually averaged distributions of τ_a and TOA $F_{ari}^{cloud-free}$ obtained from an aerosol reanalysis are shown in Figure 5.10. These estimates correspond to a TOA $F\ aricloud-free$ by total aerosol of −7.3 W m^{-2}. 40% of that total is exerted by anthropogenic aerosols (including biomass burning aerosols, see Box 5.2), 38% by marine aerosols, 19% by mineral dust aerosols, and 3% by land-based biogenic aerosols. Negative $F_{ari}^{cloud-free}$ generally correspond to high τ_a, except over reflective deserts where $F_{ari}^{cloud-free}$ is a balance between a negative contribution from a large mineral dust loading (ϖ_0~0.98) and a positive contribution from a small amount of transported anthropogenic aerosol ($\varpi_0 = 0.86$~0.98). The different signs result from interactions of aerosol absorption and surface reflectance as discussed in Section 5.2.3.

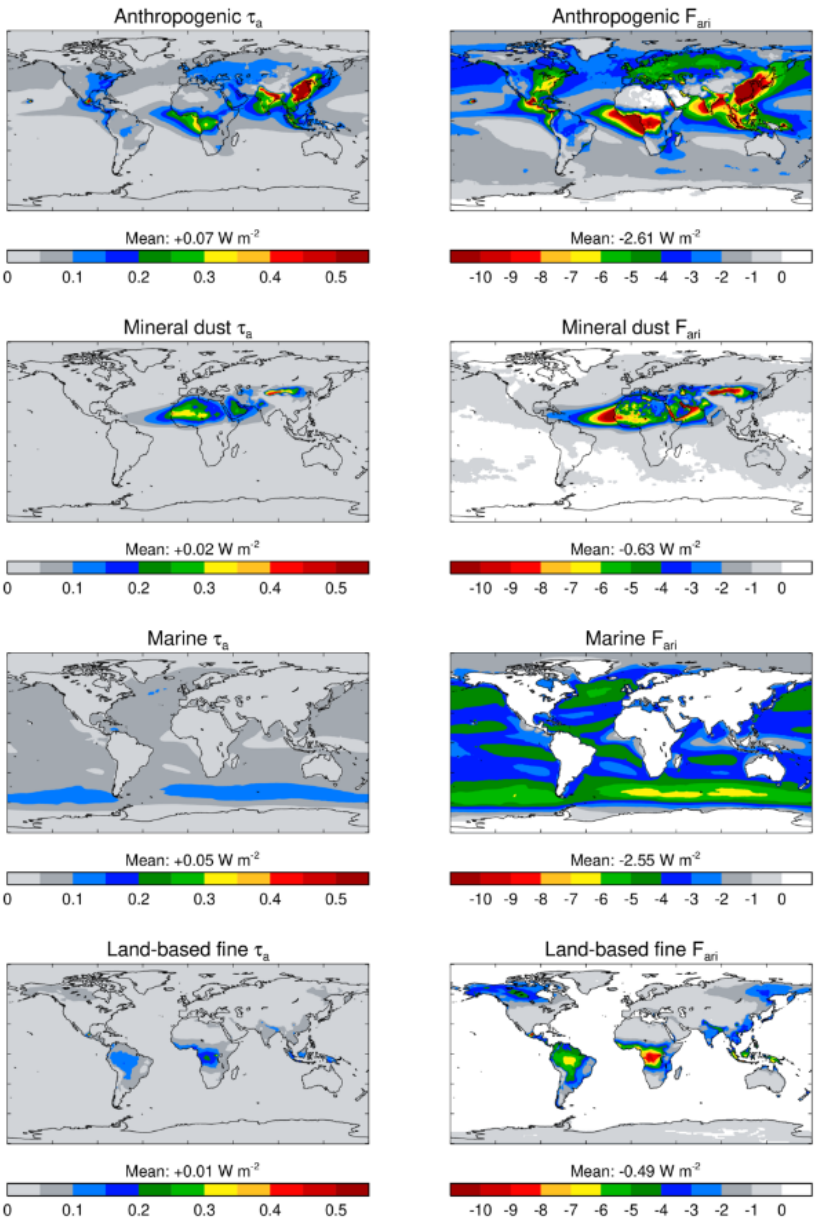

Figure 5.10. Distributions of (left) optical depth at 0.55 μm, τ_a, and (b) top-of-atmosphere, cloud-free, solar radiative effect of aerosol-radiation interactions, F_{ari} in W m^{-2}, for (top to bottom) anthropogenic, mineral dust, marine, and land-based fine-mode aerosols. Distributions are averaged over the period 2003-2019 from the CAMS reanalysis of atmospheric composition, which assimilates satellite retrievals of total aerosol optical depth.

Because of their large size, mineral dust exerts significant extinction in the terrestrial spectrum and is one of a few aerosol types with detectable signal in the atmospheric window (8-12 μm) -- see Ch. 2. Recent observations suggest that mineral dust extinction in the window region is about 70% of that in the mid-visible wavelength.

5.3.3 Aerosol-radiative effect in cloudy conditions

Observational estimates of F_{ari}^{cloudy} have only become possible recently with the first satellite retrievals of above-cloud aerosol τ_a and, in some cases, ϖ_0 (Yu and Zhang, 2013). Studies have often focused on the south-eastern Atlantic Ocean off the coast of southern Africa where biomass burning smoke overlies stratocumulus (Chand et al., 2009; Peters et al., 2011; De Graff et al., 2014; Mayer et al., 2013). F_{ari}^{cloudy} is difficult to simulate in that region because of difficulties in characterizing both aerosol and

clouds (Stier et al., 2013; Zuidema et al. 2016). More recently, studies have combined above-cloud τ_a from space lidar measurements and cloud properties from passive sensors to estimate F_{ari}^{cloudy} globally (Zhang et al., 2014; Zhang et al., 2016; Kacenelenbogen et al., 2019).

Figure 5.11 shows 8-year average distributions of annual-mean solar F_{ari}^{cloudy} at TOA and its radiative efficiency. Mineral dust and anthropogenic aerosols exert TOA F_{ari}^{cloudy} of opposite signs because of compounded differences in aerosol absorption and underlying cloud optical depth. In this example, TOA F_{ari}^{cloudy} is +0.015 (−0.03 to +0.06) W m^{-2} on a global ocean average.

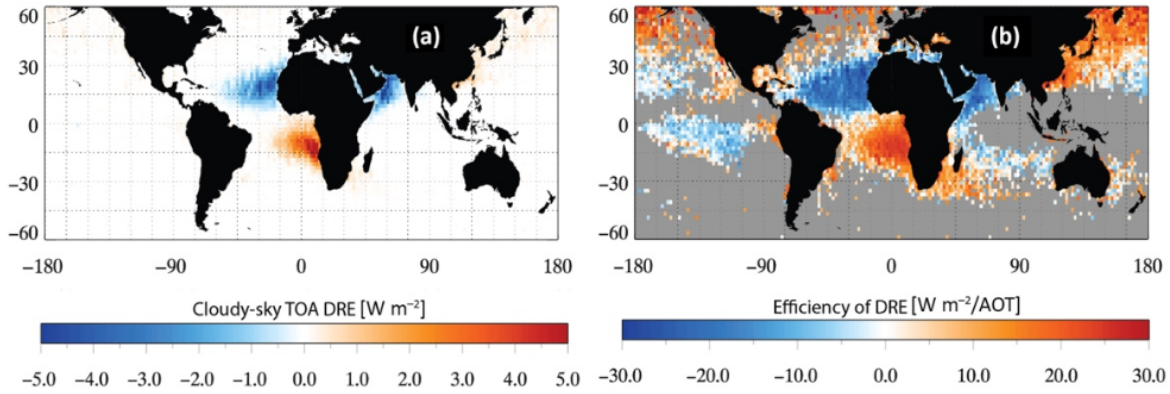

Figure 5.11. Distributions of annual mean cloudy-sky (a) solar aerosol radiative effect (W m^{-2}), and (b) its radiative effect efficiency for above-cloud aerosol as derived from 8 years of CALIOP observations. Figure adapted from Fig. 16 in Zhang et al. (2016).

5.3.4 Aerosol-radiative effect in all-sky conditions

Satellite-based estimates of solar F_{ari} are summarized in Figure 5.12. Because of the difficulty of quantifying F_{ari}^{cloudy}, there are fewer estimates than for $F_{ari}^{cloud-free}$ (Figure 5.9). Some studies simply assume that $F_{ari}^{cloudy} = 0$ and scale their estimate of $F_{ari}^{cloud-free}$ locally, applying Equation 5.26 to obtain F_{ari}. The average of all estimates is −1.97 ± 0.66 W m^{-2} at the TOA and −5.96 ± 0.69 W m^{-2} at the surface. Compared to recent estimates of the Earth's energy budget (Stephens et al. 2012), those numbers imply that aerosols increase outgoing solar flux at the TOA by about 2% and decrease incoming solar flux at the surface by about 3%. Compared to estimates of $F_{ari}^{cloud-free}$ at the TOA, the presence of clouds reduces global-mean F_{ari} by about 50% and 30% at the TOA and surface, respectively.

Estimates of F_{ari} in the terrestrial spectrum, which is exerted by coarse-mode aerosol like mineral dust and sea salt, are few. They suggest that mineral dust aerosol with particles diameters larger than 10 μm contribute a longwave F_{ari} that completely offsets the mineral dust solar F_{ari} (Kok et al., 2017; Di Biago et al. 2020) and offsets about 10% of total aerosol F_{ari}.

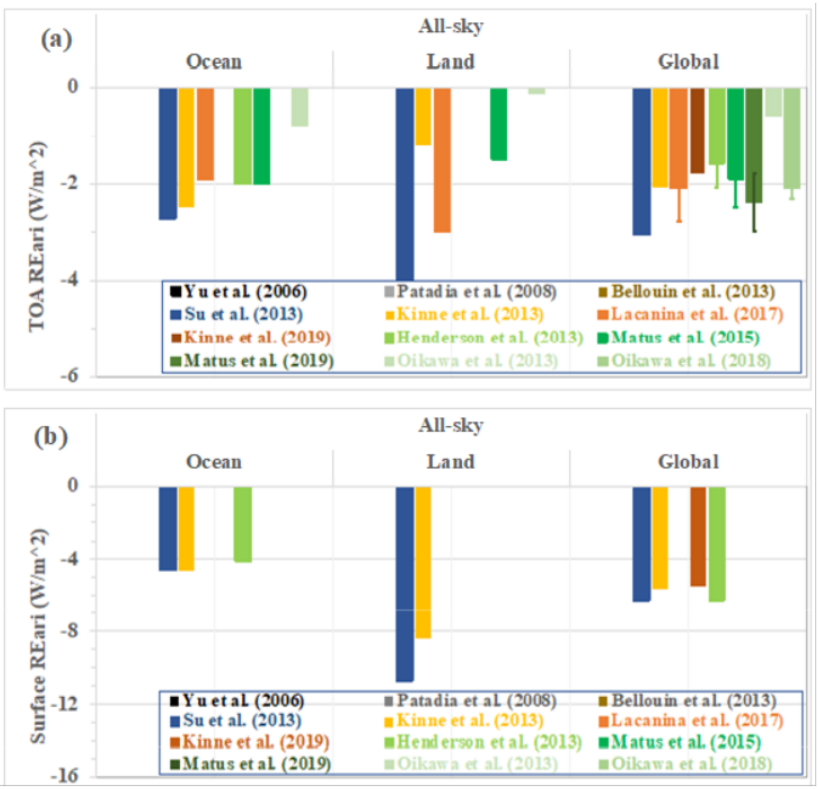

Figure 5.12 As Figure 5.9, but for all-sky conditions. Estimates are made at the (a) top of atmosphere and (b) surface.

5.4. Radiative forcing and effective radiative forcing of aerosol-radiation interactions

Radiative forcing of aerosol-radiation interactions, noted here ΔF_{ari} and quantified in W m^{-2}, is the change in F_{ari} due to human activities. Two subtly different definitions of ΔF_{ari} are used in the scientific literature, echoing similar ambiguities in the definition of anthropogenic aerosols (Box 5.2). The first, mostly used by the observation community, evaluates ΔF_{ari} from present-day distributions as the difference between total F_{ari} and that due to natural aerosols alone.

$$\Delta F_{ari} = F_{ari} - F_{ari}^{natural} \quad 5.27$$

Applying Equation 5.27 requires the ability to distinguish the natural from the anthropogenic origin of the aerosol, which is difficult from observations alone (Box 5.2). The second definition is used by the modelling community and was formalised by a series of Assessment Reports of the Intergovernmental Panel on Climate Change. It defines ΔF_{ari} as the difference in radiative fluxes between present-day and a preindustrial reference year, conventionally 1750, 1850, or the average over 1850-1900:

$$\Delta F_{ari} = F_{ari}^{present} - F_{ari}^{preindustrial} \quad 5.28$$

Equation 5.28 requires an estimate of F_{ari} in preindustrial conditions. However, preindustrial aerosol optical properties were not observed, so this second definition is only accessible to models. The second definition produces ΔF_{ari} about 40% weaker than the first (Bellouin et al. 2008), because some preindustrial aerosols were already emitted by human activities, especially biomass burning.

In addition to different reference periods for the forcing calculation, there are two definitions of ΔF_{ari} that account for different radiative effects. We use the symbol ΔF_{ari} to define the instantaneous radiative forcing caused solely by the radiative effect of a change in aerosol without any other changes to the atmosphere. The instantaneous radiative effect is altered by rapid adjustments of the atmospheric state (section 5.2.6) that occur without a large-scale change in surface temperature. To denote the *effective* radiative forcing that accounts for these adjustments we use the symbol ΔF_{ari}^{eff}.

5.4.1 Simplified expressions

Early quantifications of ΔF_{ari} relied on simplified expressions that approximated the albedo of the combined aerosol-surface system by a simple multiple reflection model (Charlson et al., 1991; Chylek and Coakley, 1974), later also accounting for aerosol absorption (Haywood and Shine, 1995).

Global, annual mean TOA ΔF_{ari} is approximated by

$$\Delta F_{ari} = -DS_0T_{at}^2(1-f_{cloud})\,\underline{\beta}_{anth}\,\tau_{a,anth} \times \left[(1-R_s)^2 - \frac{2R_s}{\underline{\beta}_{anth}}\left(\frac{1}{\varpi_0^{anth}} - 1\right)\right] \qquad 5.29$$

where D is the daylight fraction ($\frac{1}{2}$ on a global and annual average), S_0 is the solar constant (about 1361 W m^{-2}), T_{at} is the cloud- and aerosol-free atmospheric transmittance (about 0.76), f_{cloud} is the fractional cloudiness, and R_s is the surface reflectance. $\tau_{a,anth}$ and ϖ_0^{anth} are the optical depth and single-scattering albedo of anthropogenic aerosol. The upscatter fraction (Section 5.1.2.3) of anthropogenic aerosol is calculated for an average solar zenith angle and denoted here $\underline{\beta}_{anth}$.

Figure 5.13 illustrates the dependence of ΔF_{ari} at TOA on ϖ_0^{anth} and R_s. For purely scattering aerosol, the last term of Equation 5.29 vanishes and ΔF_{ari} is negative, leading to a cooling of the Earth-atmosphere system. In contrast, the sign of ΔF_{ari} exerted by partially absorbing aerosol can be negative (cooling) or positive (warming), depending on the values of ϖ_0^{anth}, $\underline{\beta}_{anth}$, and R_s. TOA ΔF_{ari} switches sign from negative to positive at a value of ϖ_0^{anth} called critical single-scattering albedo, given by:

$$\varpi_0^{anth} = \frac{2R_s}{\beta(1-R_s)^2 + 2R_s} \qquad 5.30$$

The value of the critical single-scattering albedo decreases with increasing surface reflectance.

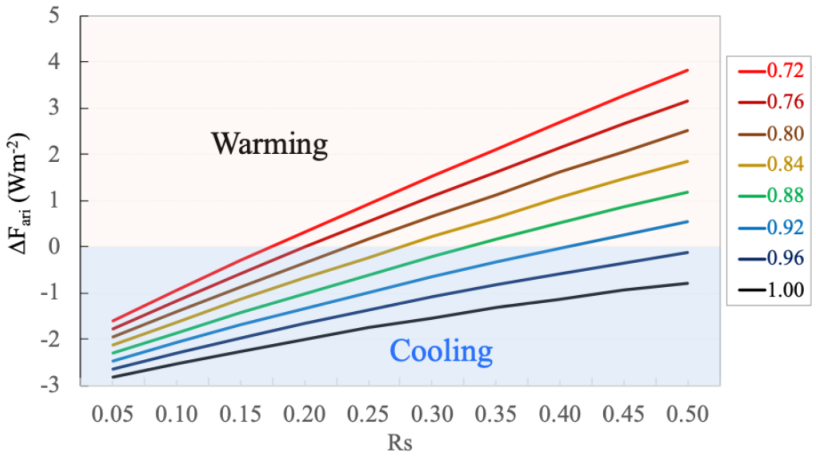

Figure 5.13: Globally and annually averaged radiative forcing of aerosol-radiation interactions, ΔF_{ari}, as calculated at the top of the atmosphere by Equation 5.29, and as a function of the single-scattering albedo of anthropogenic aerosol, ϖ_0^{anth}, (coloured lines) and the reflectance of the surface, R_s (x

axis). The anthropogenic aerosol optical depth is set to $\tau_{a,anth}$= 0.1 and the anthropogenic aerosol upscatter fraction is set to $\underline{\beta}_{anth}$ = 0.20. The fractional cloudiness is assumed be f_{cloud} = 0.7.

These simplified expressions are built on several assumptions. The aerosol layer is assumed to be optically thin ($\tau_a \ll 1$), neglecting multiple scattering within the aerosol layer. The dependence of β on θ_s (Section 5.2.2) is not considered. Geographical variations of all the parameters are not considered and therefore Equation 5.29 only applies to the global mean or a specific location. All wavelength-dependent parameters, including aerosol properties and surface reflectance, are spectrally weighted. These spectrally weighted averages are difficult to calculate because of complex interactions between aerosol and surface. Despite these assumptions, these expressions have provided important insights into the role of aerosol in perturbing the Earth's energy budget and its dependence on the aerosol optical properties (Charlson et al., 1991; Haywood and Shine, 1995; Sheridan and Ogren, 1999).

5.4.2 Industrial-era changes in aerosol radiative properties

Human activities have substantially increased during the industrial revolution, resulting in increased emissions of aerosol particles and precursor gases. Changes in aerosol amount and properties over the industrial era are represented as the difference between the present-day and a preindustrial reference year (typically 1750 or 1850). Figure 5.14 is derived from 16 global aerosol models (Myhre et al., 2013) and suggests that τ_a has increased by 0.030 ± 0.011 since 1850. That estimate falls within the assessment of Bellouin et al. (2020a), who found that globally averaged τ_a was increased by human activities by 15% to 30% (68% confidence interval) in 2005–2015 compared to the year 1850. Models explain that increase by an increase in sulfate, followed by nitrate, biomass burning aerosol, secondary organic aerosol (SOA), and carbonaceous aerosol from burning fossil fuels and biofuels (Figure 5.15). Over the industrial era, ϖ_0 has decreased by 0.006 ± 0.004 in Myhre et al. (2013), meaning that present-day aerosol is about 12% more absorbing than pre-industrial aerosol in those models.

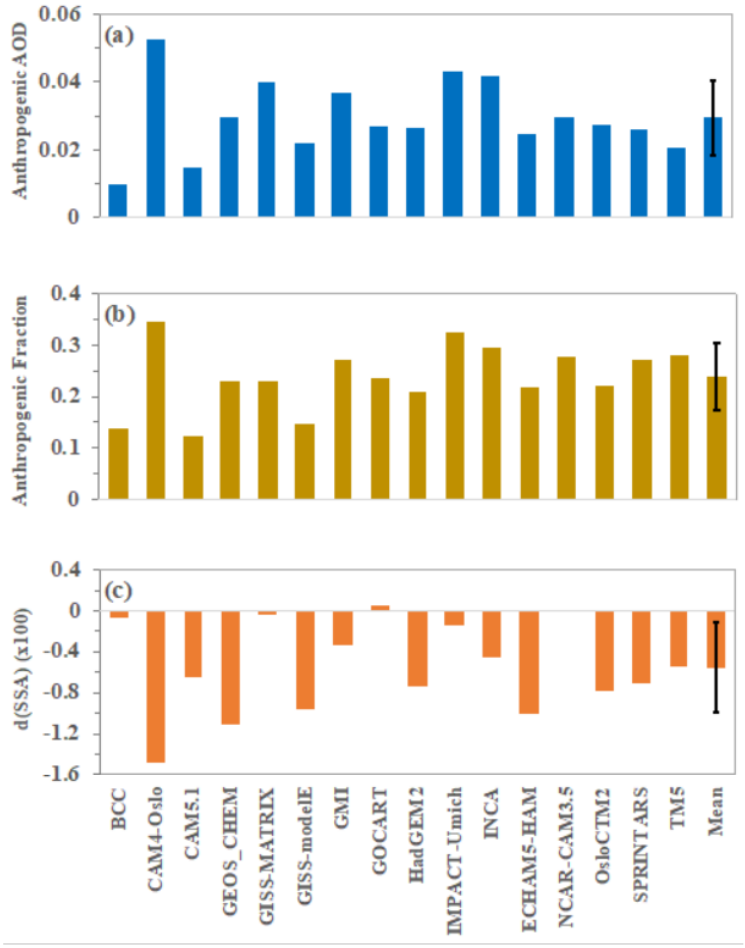

Figure 5.14 Globally averaged (a) anthropogenic aerosol optical depth (difference between 2011 and 1850), (b) anthropogenic fraction of the aerosol optical depth in 2011, and (c) changes in single-scattering albedo (x100) between 1850 and 2011 in 16 large-scale aerosol models. The last column shows the multi-model mean and its standard deviation. Both aerosol optical depth and single-scattering albedo are at a wavelength of 0.55 μm. Figure made based on Table 3 in Myhre et al. (2013).

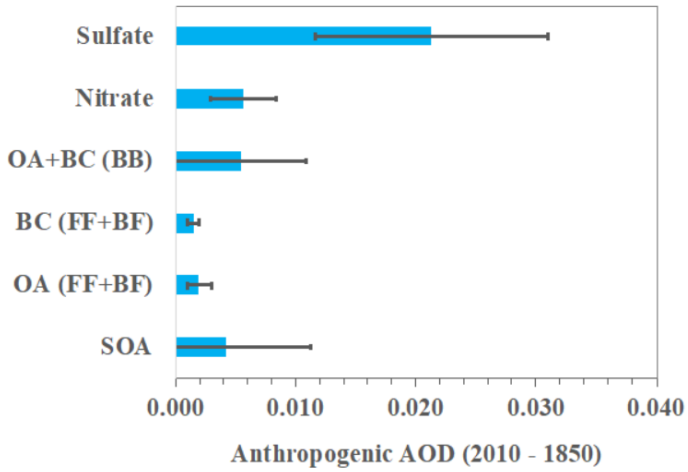

Figure 5.15 Change in anthropogenic aerosol optical depth for sulfate, nitrate, organic aerosol (OA) + black carbon (BC) from biomass burning (BB), BC and OA from burning fossil fuels (FF) and biofuels

(BF), and secondary organic aerosol (SOA) from 1850 to 2011 as simulated by the models shown in Figure 5.14.

Although the modeled temporal evolution of τ_a over the industrial era cannot be assessed with observations, continuous in situ and remote sensing measurements acquired in the recent past can be used to check the fidelity of model simulations of anthropogenic aerosol trajectories. Multi-decadal measurements of near-surface sulfur dioxide, sulfate, and black carbon concentrations are available in North America and Europe and have been used to assess model simulations (e.g., Chin et al., 2014). Satellite retrievals of τ_a and particle properties (size and shape) over the last two decades have been used to derive a proxy for the anthropogenic component (Box 5.2). Figure 5.16 compares anthropogenic τ_a retrieved from the MODIS satellite instrument with model simulations over the 2003—2016 period in the outflows of four major anthropogenic sources, West Europe, North America, East Asia, and South Asia. The model captures the observed decline in anthropogenic τ_a associated with North American and European emissions, and the increase associated with South Asian emissions during the period. However, the model does not capture the decline observed in the East Asian outflow since 2008, probably because it uses an emission dataset that underestimate the decline in Chinese aerosol emissions.

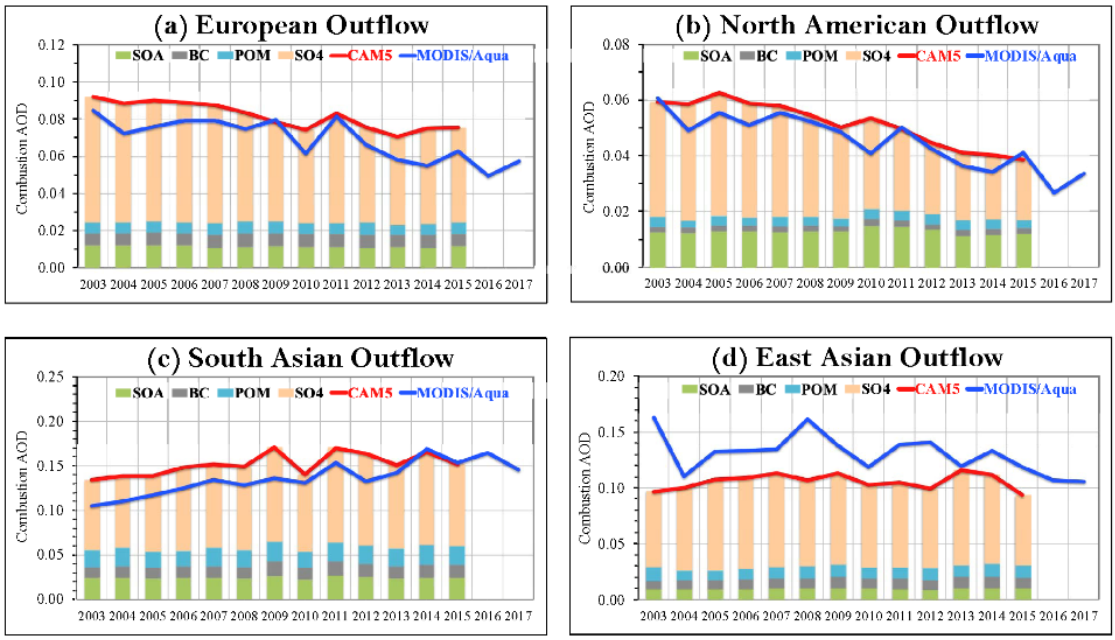

Figure 5.16 Trends of regional anthropogenic aerosol optical depth τ_a from 2003 to 2016 derived from MODIS/Aqua retrievals and CAM5 model simulations in major outflow regions: (a) European outflow (Mediterranean Sea), (b) North American Outflow (North Atlantic Ocean), (c) East Asian Outflow (Northwest Pacific Ocean), and (d) South Asian outflow (Bay of Bengal). Chemical component and source contributions to the outflow τ_a are derived from the CAM5 tagged source simulations. Figure adapted from Yu et al. (2020).

5.4.3 Industrial-era aerosol radiative forcing

Model estimates of ΔF_{ari} (defined by Equation 5.28) are essential because the preindustrial reference state has not been observed. Confidence in model estimates of ΔF_{ari} is built by comparing simulations of present-day total τ_a or, preferably, changes in τ_a over the satellite era, which for aerosols began in earnest in 2000 with dedicated instruments offering near-global cloud-free coverage, although some ocean-based retrievals are available since 1979. The review of aerosol radiative forcing by Bellouin et al. (2020a) notes a high level of agreement between simulations of globally averaged radiative forcing efficiency in cloud-free sky, at −15 to −20 W m^{-2} per unit τ_a, with remaining discrepancies driven by

regional differences in carbonaceous aerosol absorption. Models also agree that the net impact of clouds is to mask about two thirds of $\Delta F_{ari}^{cloud-free}$. Above-cloud ΔF_{ari} is weak on a global average.

Figure 5.17 shows an example of a time series of ΔF_{ari} at TOA from 1850 to 2014, both total aerosol and its components (Lund et al., 2018). Anthropogenic mineral dust is excluded as its role in radiative forcing is complex: only a poorly known fraction of mineral dust changes exerts a radiative forcing, with the remainder being part of the climate response through vegetation-driven changes in the bare soil fraction. Sulfate and black carbon stand out as important forcing agents. Scattering by sulfate causes a negative ΔF_{ari}, which suddenly became more negative in the 1950s and peaked in the 1990s before getting slowly weaker in the twenty-first century. The history of ΔF_{ari} follows that of the emissions of its gaseous precursor, sulfur dioxide (Chapter 16), changes in surface solar radiation (Ch. 2), and sulfate in ice cores (Ch 17). The weakening over the twenty-first century is underestimated in simulation shown because it used an emission inventory that underestimated the speed of decrease in Chinese emissions of sulfur dioxide after 2010. In contrast, black carbon emitted from fossil-fuel combustion, which is strongly absorbing, causes a positive ΔF_{ari} that has increased over the industrial-era. Other aerosol components yield a relatively weak, negative ΔF_{ari}. The net aerosol ΔF_{ari} is negative and peaked in the 1990s before weakening significantly into the twenty-first century, although the industrial-era evolution of ΔF_{ari} remains uncertain. The review by Bellouin et al. (2020a) used global aerosol models and perturbed parameter ensembles to bound ΔF_{ari} for 2005-2015 with respect to the year 1850 between −0.37 and −0.12 W m^{-2}.

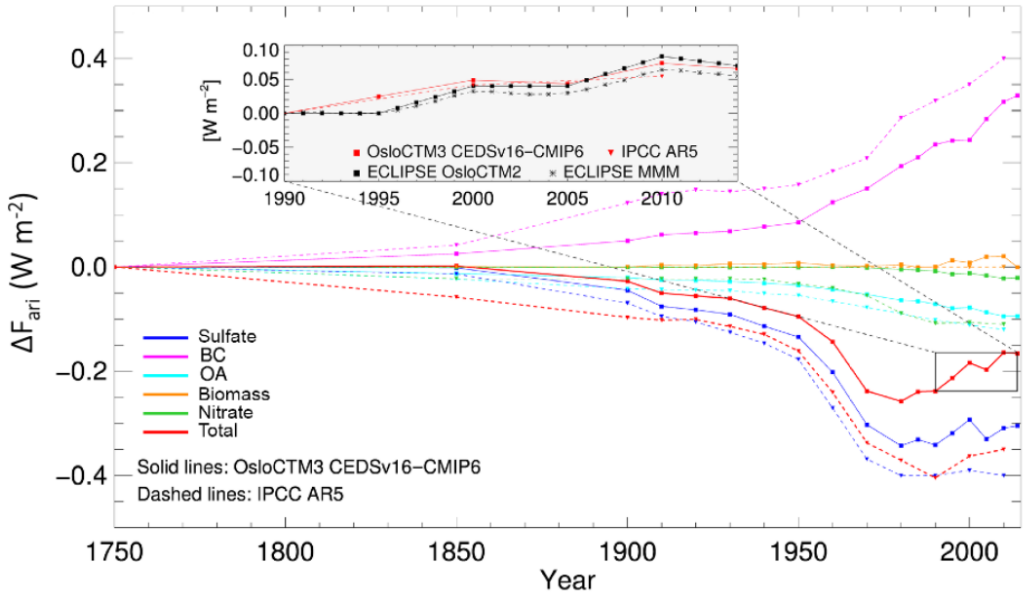

Figure 5.17 Temporal evolution of globally and annually averaged instantaneous radiative forcing of aerosol-radiation interactions, ΔF_{ari}, at the top of the atmosphere from 1750 to 2014 as simulated by the OsloCTM3 model (solid lines) and assessed in the Fifth Assessment Report of the Intergovernmental Panel on Climate Change (dashed lines). Figure adapted from Lund et al. (2018).

Observationally based estimates of ΔF_{ari} have been made by defining ΔF_{ari} with respect to present-day natural aerosols instead of the unobserved preindustrial state. In those studies, anthropogenic aerosol is distinguished from natural aerosol based on satellite retrievals of particle size and shape (Box 5.2). Figure 5.18 summarizes observational estimates of $\Delta F_{ari}^{cloud-free}$. These observation-based estimates differ by factors of more than 2. The average estimate is −1.34 ± 0.55 W m^{-2}, accounting for about one third of $F_{ari}^{cloud-free}$ by anthropogenic and natural aerosol combined. As expected from the location of anthropogenic aerosol sources, $\Delta F_{ari}^{cloud-free}$ is greater over land than over ocean. A few studies attempted to scale $\Delta F_{ari}^{cloud-free}$, mostly by assuming no contribution to ΔF_{ari} from cloudy sky. Under that assumption, the observationally based estimate of global annual mean TOA ΔF_{ari} is −0.55 ± 0.17 W m^{-2}. That is equivalent to a cloud masking of 60%, similar to the model estimates discussed

in the first paragraph of this section. The fact that observationally based estimates of ΔF_{ari} tend to be more negative than model estimates comes from the importance of the preindustrial baseline (Bellouin et al., 2008) and from industrial-era changes in aerosol absorption (Myhre, 2009) that are only accessible to large-scale models.

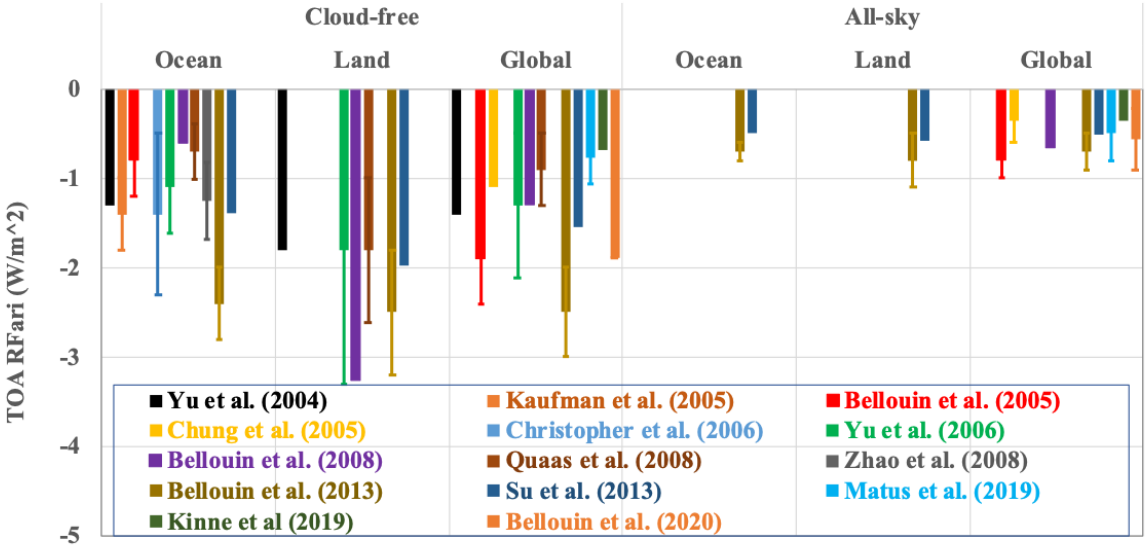

Figure 5.18 Estimates of nearly global (60°S-60°N), annual mean cloud-free solar radiative forcing of aerosol-radiation interactions at the top of the atmosphere by present-day anthropogenic aerosol with respect to present-day natural aerosols. The studies listed are based on satellite measurements of aerosol optical depth and particle properties complemented by satellite observations of radiative fluxes or aerosol intensive properties from surface observations and/or model simulations.

5.4.4. Effective radiative forcing

The effective radiative forcing ΔF_{ari}^{eff} accounts for rapid adjustments to aerosol-radiation interactions, as discussed in section 5.2.6. Based on global modelling, the review of Bellouin et al. (2020a) bounded rapid adjustments to aerosol-radiation interactions between −0.25 and −0.06 W m^{-2} at the 68% confidence level. The ΔF_{ari}^{eff} is the sum of those adjustments and the instantaneous ΔF_{ari} discussed in section 5.4.3, and is bounded by −0.58 and −0.23 W m^{-2} according to Bellouin et al. (2020a). That suggests that a quarter to a half of global mean ΔF_{ari}^{eff} is exerted by rapid adjustments, although they can represent a larger fraction in cloudy regions where absorbing aerosols are present.

Current large-scale models simulate a relatively vertically uniform heating from aerosol absorption with significant heating in the upper troposphere. As a result, models yield negative rapid adjustments that are primarily driven by decreased high-level clouds and enhanced cooling in the terrestrial spectrum (Stjern et al., 2017; Myhre et al., 2018). However, observations show different heating profiles that peak in the lower troposphere and decay to zero in the mid-troposphere. Simulations constrained with observed heating profiles obtain positive rapid adjustments associated with a significant decrease in low-and mid-level clouds and a weaker decrease in high-level clouds (Allen et al., 2019).

Box 5.2: Anthropogenic aerosols

Anthropogenic aerosol is aerosol produced by human activities. That seemingly simple definition hides two different views of what constitutes anthropogenic aerosol. The first view, common in the observational community, sees them as an aerosol type. The second view, widespread in the climate modelling community, sees them as a historical change in aerosol amounts.

When viewed as an aerosol type, anthropogenic aerosol is also called industrial or urban aerosol (e.g. Figure 5.6). Anthropogenic aerosol is broadly related to combustion processes. These processes generate aerosol particles that are small (large Ångström exponent and fine-mode fraction of the optical depth), spherical (small non-spherical fraction and depolarization ratio), and moderately absorbing. Those physical characteristics have been used as indicators of the anthropogenic origin of observed aerosol (e.g. Kaufman et al. 2005; Bellouin et al. 2005; Yu et al. 2020), especially over ocean where satellite aerosol retrievals are of sufficient quality. Over land, observational studies typically rely on modelled anthropogenic fractions.

The anthropogenic origin of aerosol is difficult to establish from observations alone. Non-combustion anthropogenic sources exist that do not match all the indicators listed above, for example nitrate precursor emissions from agriculture or mineral dust from cement production. Biomass burning aerosol can be from anthropogenic sources (e.g., prescribed burning associated with agricultural practices and forest management) or natural sources (e.g., wildfires ignited by lightning) but exhibit the same indicators. Similarly, mineral dust lifted from deserts by winds is natural, but human modifications to land use (desertification, irrigation) emit anthropogenic mineral dust or suppress natural emissions. In addition, the same aerosol particle may be a mixture of natural and anthropogenic materials.

When viewed as a historical change in aerosol amount, anthropogenic aerosol is defined as the difference between present day and an idealised preindustrial reference time where anthropogenic activities were either absent or much reduced. To simulate that preindustrial reference, models use emission inventories scaled backward in time based on assumptions on population and technology changes. Preindustrial conditions were probably more polluted than pristine conditions with natural aerosols only, but it is difficult to be sure without observations. Paleo studies, for example based on charcoal records to estimate the occurrence of preindustrial wildfires (Marlon et al., 2016), show promise but struggle to provide global constraints. But it is plausible that early industry, agricultural activities, and wildfires already emitted aerosols of human origin in preindustrial times.

5.5 Uncertainty in aerosol-radiation interactions

5.5.1 Aerosol radiative effect

The uncertainty in the net radiative effect of all atmospheric aerosol, F_{ari}, comes from uncertainties in τ_a and in the radiative effect efficiency (Section 5.3.1). The latter comes from uncertainties in the aerosol vertical profile; in aerosol intensive properties, ϖ_0 in particular; in environmental factors (Sections 5.2.2 to 5.2.5); and in the radiative transfer modelling itself. The uncertainty is expected to span a wider range than the estimates listed in Section 5.3 because several estimates use the same observations and observational uncertainties are often not fully accounted for. Current satellite remote sensing retrievals of τ_a have a typical uncertainty of ±0.05 or 10-20%, which propagates an uncertainty of about 1 W m^{-2} to F_{ari} (Kahn et al., 2009). Uncertainties and biases also depend on limitations of passive and active remote sensing. Retrievals of τ_a are generally more accurate over ocean than over land (Yu et al., 2006) and in cloud-free conditions than in cloudy conditions. Geostationary retrievals are more uncertain than polar-orbiting measurements, but measure aerosol daytime variations, which are important to quantify regional F_{ari}. Thermal infrared τ_a is observed only by a limited number of sensors, adding uncertainty in estimates of net F_{ari}.

The largest source of uncertainty in F_{ari} is ϖ_0 (Loeb and Su, 2010) but more-accurate retrievals remain a grand challenge and even in situ measurements are limited. The uncertainty associated with ϖ_0 retrieved from ground-based sun-photometers decreases with increasing $\tau \ \ a$, reaching about ±0.03 for $\tau_a > 0.4$ (Dubovik et al., 2000; 2002; Sinyuk et al., 2020). Satellite retrievals of ϖ_0 are only emerging and tend to be more accurate over bright surfaces, such as for above-cloud aerosol. Further improvement requires implementing new technologies. Multi-angular spectral polarimetry is especially promising (Chen et al., 2020). Although studies that combine satellite retrievals of τ_a with TOA radiative fluxes avoid the need for assumptions on ϖ_0, such estimates have only been applied for TOA F_{ari} over oceans and are subject to additional sources of uncertainty when transforming instantaneous radiance into radiative flux (Yu et al., 2009).

F_{ari} simulated by large-scale aerosol models suffers from uncertainties in the same quantities as in observational estimates, but for different reasons. Errors in emissions, transport, and removal of different aerosol species lead to errors in simulated aerosol concentrations that propagate to τ_a in complex ways, depending on the radiative efficiencies of the simulated aerosol types. However, simulated τ_a can be constrained by satellite retrievals. Such constraints have reduced differences between models, but perhaps for the wrong reasons. Model simulations of ϖ_0 are even more uncertain, hindered by the lack of observational constraints on aerosol types. Modelling the complex mixing state of aerosol and its effect on ϖ_0 is highly parameterized and subject to large uncertainties. Environmental factors and radiative transfer modelling also contribute significantly to the uncertainty in model-based estimates of F_{ari}. Uncertainties associated with surface albedo, clouds, and radiative transfer schemes can introduce a relative standard deviation of 12% and 97% in TOA F_{ari} for purely scattering ($\varpi_0 = 1$) and strongly absorbing ($\varpi_0 = 0.8$) aerosol, respectively (Stier et al. 2013). Uncertainties are particularly large in regions of stratocumulus cloud decks, deserts, or sea ice. On a radiative transfer point of view, two-stream approximations used in large-scale models are subject to persistent biases (Section 5.6.2; Randles et al. 2013).

5.5.2 Aerosol radiative forcing

Much of the uncertainty sources discussed in the previous sections for F_{ari} also apply to ΔF_{ari} and ΔF_{ari}^{eff}. Uncertainty ranges reported for ΔF_{ari} in recent assessments (IPCC, 2013; Bellouin et al., 2020a) are relatively narrow, at −0.37 to −0.12 W m^{-2} at the 68% confidence level, increasing to −0.58 to −0.23 W m^{-2} when including rapid adjustments (ΔF_{ari}^{eff}). These narrow ranges are debated because they imply that large-scale models are more certain than the uncertainty in ΔF_{ari} derived from uncertainties in satellite estimates of τ_a and ϖ_0 alone (Loeb and Su, 2010; Thorsen et al., 2020). That debate has not been solved. It is possible that observationally based estimates overestimate the uncertainty by neglecting some cancellations of biases, or that model-based estimates are overconfident.

In addition, quantifying ΔF_{ari} and ΔF_{ari}^{eff} requires either knowledge of the anthropogenic fraction of present-day τ_a when using Equation 5.27, or knowledge of industrial-era changes in τ_a and ϖ_0 when using Equation 5.28. Those additional sources of uncertainty are substantial (Bellouin et al., 2020a) and difficult to reduce based on observations alone (Box 5.2).

5.6 Modelling

Models represent aerosol-radiation interactions in very diverse ways, strongly depending on the sophistication of the representation of aerosols and of radiative transfer.

5.6.1 Dependence on aerosol representations

At the complex end of the scale in terms of current aerosol representations are two-moment aerosol-climate models, which resolve mass and number concentrations of several aerosol components (Chapter 4, Vignati et al. 2004). These models resolve the particle size distribution, commonly assuming three or four soluble and insoluble modes represented by lognormal number size distribution functions of varying mean radius, but fixed standard deviations. For soluble modes, hygroscopic growth increases the mean particle radius. The various chemical species (sulfate, black carbon, etc.) are generally assumed to be internal within modes, meaning that an average refractive index needs to be calculated. There is a choice of mixing rules to perform those calculations, from simple volume-weighted averaging to core-shell approaches, where a solid particle core is coated with liquid (Stier et al. 2007). For soluble modes, the refractive index of the water taken up by the particles needs to be account for in the calculation. Mie theory is used once the size distribution and refractive index of the mixture are known to calculate specific scattering and absorption coefficients and the asymmetry factor. T-matrix approaches are used in some models for non-spherical particles. Specific coefficients, in m^2 kg^{-1}, are chosen because they combine naturally with particle masses expressed as mass mixing ratios, in

kg[particles] kg [dry air]$^{-1}$. The cost of performing Mie calculations over large horizontal, vertical, and spectral domains is however prohibitive, so the calculations are typically performed beforehand for realistic combinations of size distributions and real and imaginary parts of the refractive index and stored in look-up tables (e.g. Stier et al., 2005; Bellouin et al., 2013). The internally mixed nature of two-moment models complicates the calculation of component aerosol optical depths because the specific coefficients of a given component are affected by the other components. Consequently, component optical depths need to be scaled to add up to the total aerosol optical depth.

One-moment aerosol models, also called bulk-mass aerosol models, are simpler as they only simulate the particle mass concentration for a selection of externally mixed components. Such models are used in some climate models, chemistry-transport models, or large eddy simulations. Size distribution, refractive index, and hygroscopic growth curves are prescribed globally for each component, meaning that the specific scattering and absorption coefficient are fixed, and again Mie calculations can be done beforehand and stored in look-up tables (e.g., Bellouin et al. (2011)). The calculation of component optical depths in one-moment models is straightforward.

At the simpler end of the scale are models that do not represent aerosols interactively: instead their mass concentrations or even their optical properties are prescribed as fixed or time-varying three-dimensional distributions. For models that prescribe mass concentrations, aerosol-radiation interactions are calculated as in the case of bulk-mass models. For models that prescribe optical properties, the distributions of specific absorption and scattering coefficients and asymmetry factor are direct inputs to the radiative transfer model (e.g., Stevens et al. 2017).

5.6.2 Dependence on approximations used in radiative transfer

Different numerical methods are available to solve the radiative transfer equation in multiply scattering atmospheres (Hansen and Travis 1974): adding-doubling, successive orders of scattering, discrete ordinate method, or Monte-Carlo approaches, to list just a few. The successive orders of scattering and discrete ordinate methods are particularly popular choices thanks to the availability of well-tested, numerically stable algorithms (Vermote et al., 1997; Stamnes et al. 1988). The discrete ordinate method decomposes the radiative transfer problem into a finite number of directions and requires the aerosol phase function to be decomposed in its Legendre moments L_n:

$$L_n = \frac{2n+1}{2} \int_{-1}^{1} P(\ cos\ \Theta)\, P_n(\ cos\ \Theta')\, d\ cos\ \Theta \qquad 5.31$$

where P_n are Legendre polynomials. Because the phase function presents a very strong forward peak (section 5.1.2.3), it is mathematically efficient to first apply the so-called Delta-Eddington approximation and truncate that peak away, rescaling the optical properties accordingly (Joseph et al. 1976). In the past, a simplified form of the phase function, called the Henyey-Greenstein phase function, was popular. That phase function is written

$$P_{HG}(\Theta) = \frac{1-g^2}{(1+g^2-2g\ cos\ \Theta\ )^{3/2}} \qquad 5.32$$

and has the interesting feature that its Legendre moments are simply $L_n = g^n$. But concerns over its accuracy (Boucher 1998) and the availability of faster computers have made that practice rarer. Nevertheless, the cost of radiative transfer calculations remains a consideration for many applications, especially large-scale climate modelling. Those models currently use the two-stream approximation of the discrete ordinate method, thus only resolving radiative fluxes in the upward and downward directions. Only the first two moments of the Legendre decomposition of the aerosol phase function are required in that approximation, and they are simply $L_0 = 1$ and $L_1 = 3g$.

5.6.3 Model evaluation

Aerosol-radiation interactions are extremely useful to evaluate models because several aerosol optical properties can be retrieved from remote-sensing measurements. Ground-based networks, for example the Aerosol Robotic Network (AERONET; Holben et al. 1998), and several passive and active satellite

sensors (e.g., Kaufman et al., 2002; Kahn, 2012) routinely retrieve the aerosol optical depth and, with more difficulty so in a more limited number of cases, the aerosol single-scattering albedo. Since those quantities are defined reasonably consistently in models and easily diagnosed, by applying Equations 5.18 and 5.21, they provide great opportunities to evaluate aspects of simulated aerosol radiative effects and forcing. Note that models do not need to have a radiative transfer code to compute aerosol optical depth, so chemical-transport models provide it too: Equation 5.18 is only based on aerosol physical and optical properties.

Aerosol optical depth is a demanding quantity to simulate correctly, as it depends on particle mass, size distribution, and chemical composition. It is however possible to get the correct aerosol optical depth for the wrong reasons as errors in those three aspects may compensate. Adding additional constraints, for example also comparing the single-scattering albedo or Ångstrøm exponent, reduces the possibility for misleading compensations. Figure 5.19 shows the median distribution of the aerosol optical depth at 0.55 μm simulated by 20 global aerosol models that participated in the AeroCom I inter-comparison exercise (Kinne et al., 2006), compared to a composite of 4 satellite retrievals of aerosol optical depth. Although models simulate the correct qualitative pattern, differences in magnitude appear in several regions. Large-scale models also disagree quantitatively with each other in their simulated aerosol optical depth and single-scattering albedo, both regionally and on a global average, and both seasonally and on an annual average.

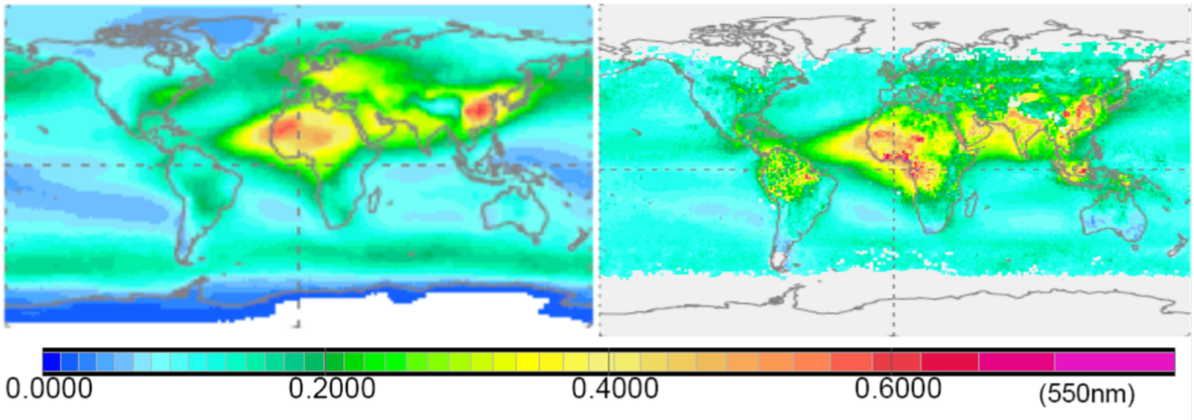

Figure 5.19. Annually averaged aerosol optical depth at 0.55 μm of (left) the median of 20 large-scale aerosol model AeroCom I simulations and (right) a composite of 4 satellite retrievals, with the best retrieval selected in different regions for agreement with sun-photometer measurements. Adapted from figures 5 and A1 of Kinne et al. (2006).

Another difficulty is that aerosol remote sensing retrievals are more uncertain, and in some cases impossible, when aerosols do not dominate the measured radiance, i.e. in cases of low aerosol optical depth, cloudy skies, or bright surfaces. The global aerosol distribution is therefore incompletely sampled by observations, leading to possibly misleading comparisons against models (Schutgens et al. 2017). A robust comparison also requires temporal collocation between model data and observations, but that involves high-frequency output from models, greatly increasing data size. Satellite simulators, like COSP (Cloud Feedback Model Intercomparison Project Observation Simulator Package; Bodas-Salcedo et al., 2011), which try to reproduce retrievals conditions in models, have been developed as a work around. Finally, the modelling and remote-sensing community have different views on what constitutes an aerosol type, in part because not all physical and chemical characteristics of aerosols are accessible to observations. These differences often prevent like-for-like comparisons between simulated and observed aerosol properties. (See also Chapter 15.) Further examples of model-observation comparison are provided in the modelling section of Chapter 15.

Bibliography

Ackerman, A. S., Toon, O. B., Stevens, D. E., Heymsfield, A. J., Ramanathan, V., Welton, E. J., 2000. Reduction of tropical cloudiness, Science, 288,1042-1047, doi:10.1126/science.288.5468.1042.

Allen, R. J., Amini-Farahani, A., Lamarque, J.-F., Smith, C., Shindell, D., Hassan, T., et al., 2019. Observationally constrained aerosol-cloud semi-direct effcts, NPJ Climate and Atmospheric Science, 2:16, https://doi.org/10.1038/s41612-019-0073-9.

Bellouin, N., Boucher, O., Vesperini, M., Tanré, D., 2004. Estimating the direct aerosol radiative perturbation: Impact of ocean surface representation and aerosol non-sphericity. Quarterly Journal of the Poyal Meteorological Society., 130, 2217-2232, doi:10.1256/qj.03.136.

Bellouin, N., Boucher, O., Haywood, I., Reddy, M. S., 2005. Global estimate of aerosol direct radiative forcing from satellite measurements, Nature, 438, 1138-1141, doi:10.1038/nature04348.

Bellouin, N., Jones, A., Haywood, J., Christopher, S. A., 2008. Updated estimate of aerosol direct radiative forcing from satellite observations and comparison against the Hadley Centre climate model, Journal of Geophysical Research, 113, D10205, doi:10.1029/2007JD009385.

Bellouin, N., Rae, J., Jones, A., Johnson, C., Haywood, J., Boucher, O., 2011. Aerosol forcing in the Climate Model Intercomparison Project (CMIP5) simulations by HadGEM2-ES and the role of ammonium nitrate, Journal of Geophysical Research, 116, D20206, doi:10.1029/2011JD016074.

Bellouin, N., Mann, G. W., Woodhouse, M. T., Johnson, C., Carslaw, K. S., Dalvi, M., 2013. Impact of the modal aerosol scheme GLOMAP-mode on aerosol forcing in the Hadley Centre Global Environmental Model, Atmospheric Chemistry and Physics, 13, 3027–3044, https://doi.org/10.5194/acp-13-3027-2013.

Bellouin, N., Quaas, J., Gryspeerdt, E., Kinne, S., Stier, P., Watson-Parris, D., et al., 2020a. Bounding global aerosol radiative forcing of climate change. Reviews of Geophysics, 58, e2019RG000660, (2020a). https://doi.org/10.1029/2019RG000660.

Bellouin, N., Daviews, W., Shine, K. P., Quaas, J., Mulmenstadt, J., Forster, P. M., et al., 2020b. Radiative forcing of climate change from the Copernicus reanalysis of atmospheric composition, Earth System Science Data, 12, 1649-1677.https://doi.org/10.5194/essd-12-1649-2020.

Bodas-Salcedo, A., Webb, M. J., Bony, S., Chepfer, H., Dufresne, J., Klein, S. A., et al., 2011. COSP: Satellite simulation software for model assessment. The Bulletin of the American Meteorological Society, 92, 1023–1043, https://doi.org/10.1175/2011BAMS2856.1

Bohren, C.F., and Huffman, D.R, 1998. Absorption and Scattering of Light by Small Particles. 530 pages. John Wiley, Hoboken, New Jersey. ISBN: 9780471293408. https://doi.org/10.1002/9783527618156.

Bond, T. C., Doherty, S. J., Fahey, D. W., Forster, P. M., Berntsen, T., DeAngelo, B. J., et al., 2013. Bounding the role of black carbon in the climate system: A scientific assessment, Journal of Geophysical Research, 118, 5380-5552, https://doi.org/10.1002/jgrd.50171.

Boucher, O., 1998. On Aerosol Direct Shortwave Forcing and the Henyey–Greenstein Phase Function. Journal of the Atmospheric Sciences, 55, 128–134, https://doi.org/10.1175/1520-0469(1998)055<0128:OADSFA>2.0.CO;2

Carslaw, K. S., Lee, L. A., Reddington, C. L., Pringle, K. J., Rap, A., Forster, P. M., et al., 2013. Large contribution of natural aerosols to uncertainty in indirect forcing, Nature, 503, 67-71. https://doi.org/10.1038/nature12674.

Chand, D., Wood, R., Anderson, T. L., Satheesh, S. K., Charlson, R. J., 2009. Satellite-derived direct radiative effect of aerosols dependent on cloud cover, Nature Geoscience, 2, 181-184. doi:10.1038/NGEO437.

Charlson, R. J., Langner, J., Rodhe, H., Leovy, C. B., Warren, S. G., 1991. Perturbation of the northern hemisphere radiative balance by backscattering from anthropogenic sulfate aerosols. Tellus-A, 43, 152-163, doi:10.1034/j.1600-0870.1991.00013.x.

Charlson, R. J., Schwartz, S. E., Hales, J. M., Cess, R. D., Coakley, J. A., Hansen, J. E., et al., 1992. Climate forcing by anthropogenic aerosols. Science, 255, 423-430, doi:10.1126/science.255.5043.423.

Chen, C., Dubovik, O., Fuertes, D., Litvinov, P., Lapyonok, T., Lopatin, A., Ducos, F., Derimian, Y., Herman, M., Tanré, D., Remer, L. A., Lyapustin, A., Sayer, A. M., Levy, R. C., Hsu, N. C., Descloitres, J., Li, L., Torres, B., Karol, Y., Herrera, M., Herreras, M., Aspetsberger, M., Wanzenboeck, M., Bindreiter, L., Marth, D., Hangler, A., and Federspiel, C, 2020. Validation of GRASP algorithm product from POLDER/PARASOL data and assessment of multi-angular polarimetry potential for aerosol monitoring, Earth Syst. Sci. Data, 12, 3573–3620. https://doi.org/10.5194/essd-12-3573-2020

Chin, M., Diehl, T., Tan, Q., Prospero, J. M., Kahn, R. A., Remer, L. A., et al., 2014. Multi-decadal variations of atmospheric aerosols from 1980 to 2009: Sources and regional trends, Atmospheric Chemistry and Physics, 14, 3657-3690, doi:10.5194/acp-14-3657-2014.

Chylek, P., Coakley, J., 1974. Aerosol and climate, Science, 183, 75-77. DOI: 10.1126/science.183.4120.75.

de Graaf, M., Bellouin, N., Tilstra, L. G., Haywood, J., Stammes, P., 2014. Aerosol direct radiative effect of smoke over clouds over the southeast Atlantic Ocean from 2006 to 2009, Geophysical Research Letters, **41**, 21, 7723-7730. doi:10.1002/2014GL061103.

Derimian, Y., O. Dubovik, X. Huang, T. Lapyonok, P. Litvinov, A. Kostinski, P. Dubuisson, and F. Ducos, 2016. Comprehensive tool for calculation of radiative fluxes: illustration of shortwave aerosol radiative effect sensitivities to the details in aerosol and underlying surface characteristics, Atmos. Chem. Phys., 2016, 16, 5763-5780. https://doi.org/10.5194/acp-16-5763-2016.

Di Biago, C., Balkanski, Y., Albani, S., Boucher, O., Formenti, P., 2020. Direct radiative effect by mineral dust aerosols constrained by new microphysical and spectral optical data, Geophysical Research Letters, 47, e2019GL086186, https://doi.org/10.1029/2019GL086186.

Dubovik, O., and King, M. D., 2000. A flexible inversion algorithm for retrieval of aerosol optical properties from Sun and sky radiance measurements, J. Geophys. Res., 105(D16), 20673– 20696. https://doi.org/10.1029/2000JD900282

Dubovik, O., Smirnov, A., Holben, B. N., King, M. D., Kaufman, Y. J., Eck, T. F., and Slutsker, I., 2000. Accuracy assessments of aerosol optical properties retrieved from Aerosol Robotic Network (AERONET) Sun and sky radiance measurements, J. Geophys. Res., 105(D8), 9791– 9806. https://doi.org/10.1029/2000JD900040

Dubovik, O., Holben, B. N., Eck, T., Smirnov, A., Kaufman, Y. J., King, M., et al., 2002. Variability of absorption and optical properties of key aerosol types observed in worldwide locations. Journal of the Atmospheric Sciences, 59, 590-608. DOI: https://doi.org/10.1175/1520-0469(2002)059<0590:VOAAOP>2.0.CO;2.

Hansen, J. E., Travis, L. D., 1974. Light scattering in planetary atmospheres. Space Science Review, 16, 527-610, doi:10.1007/BF00168069.

Hansen, J. E., M. Sato, M., Ruedy, R., 1997. Radiative forcing and climate response, Journal of Geophysical Research, 102, 6831-6864. https://doi.org/10.1029/96JD03436.

Haywood, J. M., Shine, K. P., 1995.The effect of anthropogenic sulfate and soot aerosol on the clear sky planetary radiation budget, Geophysical Research Letters, 22(5), 603-606, https://doi.org/10.1029/95GL00075.

Haywood, J. M., Shine, K. P., 1997. Multi-spectral calculations of the direct radiative forcing of tropospheric sulphate and soot aerosols using a column model. Quarterly Journal of Royal Meteorological Society, 123, 1907–1930. https://doi.org/10.1002/qj.49712354307.

Haywood, J. M., Allan, R. P., Culverwell, I., Slingo, T., Milton, S., Edwards, J., et al., 2005. Can desert dust explain the outgoing longwave radiation anomaly over the Sahara during July 2003? Journal of Geophysical Research, 110, D05105, doi:10.1029/2004JD005232.

Henderson, D. S., L'Ecuyer, T., Stephens, G., Partain, P., Sekiguchi, M., 2013. Multisensor perspective on the radiative impacts of clouds and aerosols, Journal of Applied Meteorology and Climatology, 52, 853-871, doi: 10.1175/JAMC-D-12-025.1.

Herbert, R. J., Bellouin, N., Highwood, E. J., Hill, A. A., 2020. Diurnal cycle of the semi-direct effect from a persistent absorbing aerosol layer over marine stratocumulus in large-eddy simulations, Atmospheric Chemistry and Physics, 20, 1317-1340. https://doi.org/10.5194/acp-20-1317-2020.

Hobbs, P. V., Reid, J. S., Kotchenruther, R. A., Ferek, R. J., Weiss, R., 1997. Direct radiative forcing by smoke from biomass burning, Science, 275, 1776-1778, doi:10.1126/science.275.5307.1777.

Holben, B. N., Eck, T.F., Slutsker, I., Tanré, D., Buis, J. P., Setzer, A., et al., 1998. AERONET—A Federated Instrument Network and Data Archive for Aerosol Characterization, Remote Sensing of Environment, 66, 1, 1-16, doi: 10.1016/S0034-4257(98)00031-5.

IPCC, 2013: Climate Change 2013: The Physical Science Basis. Contribution of Working Group I to the Fifth Assessment Report of the Intergovernmental Panel on Climate Change [Stocker, T.F., D. Qin, G.-K. Plattner, M. Tignor, S.K. Allen, J. Boschung, A. Nauels, Y. Xia, V. Bex and P.M. Midgley (eds.)]. Cambridge University Press, Cambridge, United Kingdom and New York, NY, USA, 1535 pp, doi:10.1017/CBO9781107415324.

Inness, A., Ades, M., Agusta-Panareda, A., Barre, J., Benedictow, A., Blechschmidt, A.-M., et al., 2019. The CAMS reanalysis of atmospheric composition, Atmospheric Chemistry and Physics, 19, 3515-3556. https://doi.org/10.5194/acp-19-3515-2019.

Johnson, B., Shine, K. P., Forster, P. M., 2004. The semi-direct aerosol effect: Impact of absorbing aerosols on marine stratocumulus, Quarterly Journal of Royal Meteorological Society. 130, 1407-1422. https://doi.org/10.1256/qj.03.61.

Joseph, J. H., Wiscombe, W.J., A. Weinman, J. A., 1976. The Delta-Eddington Approximation for Radiative Flux Transfer. Journal of the Atmospheric Sciences, 33, 2452–2459, https://doi.org/10.1175/1520-0469(1976)033<2452:TDEAFR>2.0.CO;2.

Kacenelenbogen, M. S., Vaughan, M. A., Redemann, J., Young, S. A., Liu, Z., Hu, Y., et al., 2019. Estimations of global shortwave direct aerosol radiative effects above opaque water clouds using a combination of A-Train satellite sensors, Atmospheric Chemistry and Physics, **19**, 7, 4933-4962. doi:10.5194/acp-19-4933-2019.

Kahn, R.A., Yu, H., Schwartz, S. E., Chin, M., Feingold, G., Remer, L. A., et al., 2009. Introduction, in Atmospheric Aerosol Properties and Climate Impacts, A Report by the U.S. Climate Change Science Program and the Subcommittee on Global Change Research. [Mian Chin, Ralph A. Kahn, and Stephen E. Schwartz (eds.)]. National Aeronautics and Space Administration, Washington, D.C., USA.

Kahn, R. A., 2012. Reducing the Uncertainties in Direct Aerosol Radiative Forcing. Surveys in Geophysics, 33 (3-4), 701-721. https://doi.org/10.1007/s10712-011-9153-z

Kaufman, Y. J., Tanré, D., Boucher, O., 2002. A satellite view of aerosols in the climate system. Nature, 419, 215–223. https://doi.org/10.1038/nature01091

Kaufman, Y. J., Boucher, O., Tanre, D., Chin, Remer, L. A., Takemura, T., 2005. Aerosol anthropogenic component estimated from satellite data, Geophysical Research Letters, 32, L17804, doi:10.0192/2005GL023125.

Keil, A., Haywood, J. M., 2003. Solar radiative forcing by biomass burning aerosol particles during SAFARI 2000: A case study based on measured aerosol and cloud properties, Journal of Geophysical Research, 108, D13, 8467, doi:10.1029/2002JD002315.

Kinne, S., Schulz, M., Textor, C., Guibert, S., Balkanski, Y., Bauer, et al., 2006. An AeroCom initial assessment – optical properties in aerosol component modules of global models, Atmospheric Chemistry and Physics, 6, 1815–1834, https://doi.org/10.5194/acp-6-1815-2006.

Kok, J. F., Ridley, D. A., Zhou, Q., Miller, R. L., Zhao, C., Heald, C. L., et al., 2017. Smaller desert dust cooling effect estimated from analysis of dust size and abundance. Nature Geoscience, **10**, no. 4, 274-278, doi:10.1038/ngeo2912.

Koren, I., Kaufman, Y. J., Remer, L. A., Martins, J. V., 2004. Measurement of the effect of Amazon smoke on inhibition of cloud formation, Science, 303, 1342-1345, doi:10.1027/science/1089424.

Kotchenruther, R. A., Hobbs, P. V., 1998. Humidification factors of aerosols from biomass burning in Brazil, Journal of Geophysical Research, 103, D24, 32-81-32089. https://doi.org/10.1029/98JD00340.

Loeb, N. G., Su, W., 2010. Direct Aerosol Radiative Forcing Uncertainty Based on a Radiative Perturbation Analysis. Journal of Climate, 23(19), 5288-5293. doi: 10.1175/2010JCLI3543.1.

Lund, M. T., Myhre, G., Haslerud, A. S., Skeie, R. B., Griesfeller, J., Platt, S. M., et al., 2018. Concentrations and radiative forcing of anthropogenic aerosols from 1750 to 2014 simulated with the Oslo CTM3 and CEDS emission inventory, Geoscience Model Development, 11, 4909-4931. https://doi.org/10.5194/gmd-11-4909-2018.

Marlon, J. R., Kelly, R., Daniau, A. L., Vannière, B., Power, M. J., Bartlein, P., et al., 2016. Reconstructions of biomass burning from sediment charcoal records to improve data-model comparisons. Biogeosciences.13(22):3225–44. https://doi.org/10.5194/bg-13-3225-2016.

Matus, A. V., L'Ecuyer, T. S., Kay, J. E., Hannay, C., Lamarque, J.-F., 2015. The Role of Clouds in Modulating Global Aerosol Direct Radiative Effects in Spaceborne Active Observations and the Community Earth System Model, Journal of Climate, 28, 2986-3003. https://www.jstor.org/stable/26194500.

Matus, A. V., L'Ecuyer, T. S., Henderson, D. S., 2019. New estimates of aerosol direct radiative effects and forcing from A-Train satellite observations, Geophysical Research Letters, 46, 8338-8346, https://doi.org/10.1029/2019GL083656.

Meyer, K., Platnick, S., Oreopoulos, L., Lee, D., 2013. Estimating the direct radiative effect of absorbing aerosols overlying marine boundary layer clouds in the southeast Atlantic using MODIS and CALIOP, Journal of Geophysical Research - Atmospheres, 10.1002/jgrd.50449, 118, 10, 4801-4815. https://doi.org/10.1002/jgrd.50449.

Mie, G., 1908. Beiträge zur Optik trüber Medien, speziell kolloidaler Metallösungen. Ann. Phys., 330: 377-445. doi:10.1002/andp.19083300302.

Mishchenko, M. I., Travis, L. D., Mackowski, D. W., 1996. T-matrix computations of light scattering by nonspherical particles: A review, Journal of Quantitative Spectroscopy and Radiative Transfer, 55, 5, 535-575, doi: 10.1016/0022-4073(96)00002-7.

Mishchenko, M. I., L. D. Travis, and A. A. Lacis, 2002. Scattering, Absorption, and Emission of Light by Small Particles, Cambridge University Press, Cambridge. ISBN 052178252. Out of print but available online at https://www.giss.nasa.gov/staff/mmishchenko/books.html

Mishchenko, M. I., 2014. Electromagnetic Scattering by Particles and Particle Groups: An Introduction, Cambridge University Press, Cambridge, ISBN: 9781139019064, 377 pages. https://doi.org/10.1017/CBO9781139019064

Myhre, G., 2009. Consistency between satellite-derived and modeled estimates of the direct aerosol effect, Science, 325, 187-190, doi:10.1126/science.1174461. DOI:10.1126/science.1174461.

Myhre, G., Samset, B. H., Schulz, M., Balkanski, Y., Bauer, S., Berntsen, T. K., et al., 2013. Radiative forcing of the direct aerosol effect from AeroCom Phase II simulations, Atmospheric Chemistry and Physics, 13, 1853-1877, doi:10.5194/acp-13-1853-2013.

Myhre, G., Kramer, R. J., Smith, C. J., Hodnebrog, O., Forster, P., Soden, B. J., et al., 2018. Quantifying the importance of rapid adjustments for global precipitation changes, Geophysical Research Letters, 45(20), 11399-11405, doi:10.1029/2018GL079474.

Oikawa, E., Nakajima, T., Inoue, T., Winker, D., 2013. A study of the shortwave direct aerosol forcing using ESSP/CALIPSO observation and GCM simulation, Journal of Geophysical Research: Atmospheres, 118, 9, 3687-3708. doi:10.1002/jgrd.50227.

Oikawa, E., Nakajima, T., Winker, D., 2018. An Evaluation of the Shortwave Direct Aerosol Radiative Forcing Using CALIOP and MODIS Observations, Journal of Geophysical Research: Atmospheres, 123, 2, 1211-1233. doi:10.1002/2017JD027247.

Peters, K., Quass, J., Bellouin, N., 2011. Effects of absorbing aerosols in cloudy skies: a satellite study over the Atlantic Ocean, Atmospheric Chemistry and Physics, 11, 1393-1404. https://doi.org/10.5194/acp-11-1393-2011.

Petty, G., 2006. A First Course in Atmospheric Radiation. Sundog Publishing, Madison, Wisconsin, ISBN-13:978-0-9729033-1-8, 452 pages, 2006.

Randles, C. A., Kinne, S., Myhre, G., Schulz, M., Stier, P., Fischer, J., et al., 2013. Intercomparison of shortwave radiative transfer schemes in global aerosol modeling: Results from the AeroCom Radiative Transfer Experiment, Atmospheric Chemistry and Physics, 13, 2347-2379, doi:10.5194/acp-13-2347-2013.

Randles, C. A., da Silva, A. M., Buchard, V., Colarco, P. R., Darmenov, A., Govindaraju, G., et al., 2017. The MERRA-2 aerosol reanalysis, 1980 onward. Part I: System description and data assimilation evaluation, Journal of Climate, 30(17), 6823-6850. https://doi.org/10.1175/JCLI-D-16-0609.1.

Remer, L. A., Kaufman, Y. J., Tanré, D., Mattoo, S., Chu, D. A., Martins, J. V., Li, R.-R., Ichoku, C., Levy, R. C., Kleidman, R. G., Eck, T. F., Vermote, E., & Holben, B. N., 2005. The MODIS Aerosol Algorithm, Products, and Validation, Journal of the Atmospheric Sciences, 62(4), 947-973. https://doi.org/10.1175/JAS3385.1

Russell, P. B., Kacenelenbogen, M., Livingston, J. M., Hasekamp. O. P., Burton, S. P., Schuster, G. L., et al., 2014. A multiparameter aerosol classification method and its application to retrievals from spaceborne polarimetry, Journal of Geophysical Research - Atmospheres, 119, 9838–9863, doi:10.1002/2013JD021411.

Schutgens, N. A. J., Gryspeerdt, E., Weigum, N., Tsyro, S., Goto, D., Schulz, M., and Stier, P., 2016 Will a perfect model agree with perfect observations? The impact of spatial sampling, Atmos. Chem. Phys., 16, 6335–6353, https://doi.org/10.5194/acp-16-6335-2016.

Sheridan, P. J., Ogren, J. A., 1999. Observations of the vertical and regional variability of aerosol optical properties over central and eastern North America, Journal of Geophysical Research, https://doi.org/10.1029/1999JD900241.

Sherwood, S.C., Bony, S., Boucher, O., Bretherton, C., Forster, P. M., Gregory, J. M., et al., 2015. Adjustments in the Forcing-Feedback Framework for Understanding Climate Change. The Bulletin of the American Meteorological Society, 96, 217–228, https://doi.org/10.1175/BAMS-D-13-00167.1

Sinyuk, A., Holben, B. N., Eck, T. F., Giles, D. M., Slutsker, I., Korkin, S., Schafer, J. S., Smirnov, A., Sorokin, M., and Lyapustin, A, 2020. The AERONET Version 3 aerosol retrieval algorithm, associated uncertainties and comparisons to Version 2, Atmos. Meas. Tech., 13, 3375–3411. https://doi.org/10.5194/amt-13-3375-2020.

Smith, C. J., Kramer, R. J., Myhre, G., Forster, P. M., Soden, B. J., Andrews, T., et al., 2018. Understanding rapid adjustments to diverse forcing agents, Geophysical Research Letters, 45, 12023-12031, https://doi.org/10.1029/2018GL079826.

Stamnes, K., Tsay, S. C., Wiscombe, W., Jayaweera, J., 1988. Numerically stable algorithm for discrete-ordinate-method radiative transfer in multiple scattering and emitting layered media, Applied Optics, 27 (12), 2502–2509. https://doi.org/10.1364/AO.27.002502.

Stephens, G., Li, J., Wild, M. et al. An update on Earth's energy balance in light of the latest global observations. Nature Geosci **5,** 691–696 (2012). https://doi.org/10.1038/ngeo1580.

Stevens, B., Fiedler, S., Kinne, S., Peters, K., Rast, S., Müsse, J., et al., 2017. MACv2-SP: a parameterization of anthropogenic aerosol optical properties and an associated Twomey effect for use in CMIP6, Geoscience Model Development, 10, 433–452, https://doi.org/10.5194/gmd-10-433-2017.

Stier, P., Feichter, J., Kinne, S., Kloster, S., Vignati, E., Wilson, J., et al.,2005. The aerosol-climate model ECHAM5-HAM, Atmospheric Chemistry and Physics, 5, 1125–1156, https://doi.org/10.5194/acp-5-1125-2005.

Stier, P., Seinfeld, J. H., Kinne, S., Boucher, O., 2007. Aerosol absorption and radiative forcing, Atmospheric Chemistry and Physics, 7, 5237–5261, doi:10.5194/acp-7-5237-2007.

Stier, P., Schutgens, N. A. J., Bian, H., Boucher, O., Chin, M., Ghan, S., et al., 2013. Host model uncertainties in aerosol radiative forcing estimates: results from the AeroCom prescribed intercomparison study, Atmospheric Chemistry and Physics, 13, 3245-3270, doi:10.5194/acp-13-3245-2013.

Stjern, C. W., Samset, B. H., Myhre, G., Forster, P. M., Hodnebrog, O., Andrews, T., et al., 2017. Rapid Adjustments Cause Weak Surface Temperature Response to Increased Black Carbon Concentrations, Journal of Geophysical Research, 122, 11,462–11,481. https://doi.org/10.1002/2017JD027326.

Strutt, J. W., 1871. On the scattering of light by small particles. Lond. Edinb. Dubl. Phil. Mag., 4, 41, 275, doi: 10.1080/14786447108640507.

Thorsen, T. J., Ferrare, R. A., Kato, S., Winker, D., 2020. Aerosol direct radiative effect sensitivity analysis, Journal of Climate, 33, 6119-6139. DOI: https://doi.org/10.1175/JCLI-D-19-0669.1.

Vermote, E. F., Tanre, D., Deuze, J. L., Herman, M., Morcette, J., 1997. Second Simulation of the Satellite Signal in the Solar Spectrum, 6S: an overview, in IEEE Transactions on Geoscience and Remote Sensing, 35(3), 675-686. doi:10.1109/36.581987.

Vignati, E., Wilson, J., Stier, P., 2004. M7: An efficient size-resolved aerosol microphysics module for large-scale aerosol transport models, Journal of Geophysical Research, 109, D22202, doi:10.1029/2003JD004485.

Volten, H., Muñoz, O., Rol, E., de Haan, J. F., Vassen, W., Hovenier, J. W., et al., 2001. Scattering matrices of mineral aerosol particles at 441.6 nm and 632.8 nm, Journal of Geophysical Research, 106(D15), 17375– 17401, doi:10.1029/2001JD900068.

Waterman, P. C., 1965. Matrix formulation of electromagnetic scattering, in Proceedings of the IEEE, 53(8), 805-812. doi:10.1109/PROC.1965.4058.

Watson-Parris, D., Bellouin, N., Deaconu, L. T., Schutgens, N. A. J. Yoshioka, M., Regayre, J. A., et al., 2020. Constraining uncertainty in aerosol direct forcing, Geophysical Research Letters, 47, e2020GL087141, https://doi.org/10.1029/2020GL0187141.

Wiscombe, W.J., 1980. Improved Mie scattering algorithms, Applied Optics, 19, 1505-1509, doi: 10.1364/AO.19.001505.

Yu, H. Liu, S. C., Dickinson, R. E., 2002. Radiative effects of aerosols on the evolution of the atmospheric boundary layer. Journal of Geophysical Research - Atmospheres, 107(D12), 4142, doi:10.1029/2001JD000754.

Yu, H., Dickinson, R. E., Chin, M., Kaufman, Y. J., Zhou, M., Zhou, L., et al., 2004. The direct radiative effect of aerosols as determined from a combination of MODIS retrievals and GOCART simulations, Journal of Geophysical Research - Atmospheres, 109, D03206, doi:10.1029/2003JD003914.

Yu, H., Kaufman, Y. J., Chin, M., Feingold, G., Remer, L. A., Anderson, T. L., et al., 2006. A review of measurement-based assessments of the aerosol direct radiative effect and forcing, Atmospheric Chemistry and Physics, 6, 613-666. https://doi.org/10.5194/acp-6-613-2006.

Yu, H., Quinn, P. K., Feingold, G., Remer, L. A., Kahn, R. A., Chin,M., et al., 2009\. Remote Sensing and In Situ Measurements of Aerosol Properties, Burdens, and Radiative Forcing, in Atmospheric Aerosol Properties and Climate Impacts, A Report by the U.S. Climate Change Science Program and the Subcommittee on Global Change Research. [Mian Chin, Ralph A. Kahn, and Stephen E. Schwartz (eds.)]. National Aeronautics and Space Administration, Washington, D.C., USA.

Yu, H., Zhang, Z., 2013. New Directions: Emerging satellite observations of above-cloud aerosols and direct radiative forcing, Atmospheric Environment, 72, 36-40, doi:10.1016/j.atmosenv.2013.02.017.

Yu, H., Yang, Y., Wang, H., Tan, Q., Chin, M., Levy, R., et al., 2020. Interannual variability and trends of combustion aerosol and dust in major continental outflows revealed by MODIS retrievals and

CAM5 simulations during 2003 – 2017, Atmospheric Chemistry and Physics, 20, 139-161, https://doi.org/10.5194/acp-20-139-2020.

Zhang, Y., Fu, R., Yu, H., Dickinson, R. E., Juarez, R. N., Chin, M., et al., 2008. A regional climate model study of how biomass burning aerosol impacts land-atmosphere interactions over the Amazon, Journal of Geophysical Research - Atmospheres, 113, D14S15, doi:10.1029/2007JD009449.

Zhang, Z., Meyer, K., Platnick, S., Oreopoulos, L., Lee, D., Yu, H., 2014. A novel method for estimating shortwave direct radiative effect of above-cloud aerosols using CALIOP and MODIS data, Atmospheric Measurement Techniques, 7, 1777-1789, doi:10.5194/amt-7-1777-1789-2014.

Zhang, Z., Meyer, K., Yu, H., Platnick, S., Colarco, P., Liu, Z., et al., 2016. Shortwave direct radiative effects of above-cloud aerosols over global oceans derived from 8 years of CALIOP and MODIS observations, Atmospheric Chemistry and Physics, 16, 2877-2900. https://doi.org/10.5194/acp-16-2877-2016.

Zhou, M., Yu, H., Dickinson, R. E., Dubovik, O., Holben, B. N., 2005. A normalized description of the direct effect of key aerosol types on solar radiation as estimated from AERONET aerosols and MODIS albedos, Journal of Geophysical Research - Atmospheres, 110, D19202, doi:10.1029/2005JD005909.